Separation and Purification Technology 344 (2024) 127110

Contents lists available at ScienceDirect

Separation and Purification Technology

journal homepage: www.elsevier.com/locate/seppur

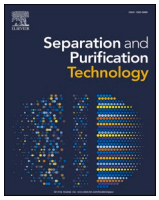

Evaluating the performance of carbon-based adsorbents fabricated from renewable biomass precursors for post-combustion CO_2 capture

Vahid Rahimi, Adrián Ferreiro-Salgado, Diego Gómez-Díaz, María Sonia Freire, Julia González-Álvarez *

Department of Chemical Engineering, School of Engineering, Universidade de Santiago de Compostela, Rúa Lope Gómez de Marzoa s/n, 15782 Santiago de Compostela, Spain

ARTICLE INFO

Keywords:
CO_2 capture
Adsorption
Biomass carbons
CO_2/N_2 selectivity
Fixed-bed simulation

ABSTRACT

The significant increase in atmospheric CO_2 concentration originated mainly from fossil fuels combustion has encouraged the development and improvement of CO_2 separation operations to reduce emissions and control climate change and global warming. Therefore, this work is focused on the separation of CO_2 from N_2 in flue gas streams under post-combustion conditions by developing low-cost adsorbents. Six carbons were fabricated from biomass resources (olive stones and almond shells) to assess their influence on CO_2 adsorption capacity: One carbonized and two KOH-activated carbons with carbon/KOH ratio of 1:2 and 1:4 (w/w) for each precursor. The carbons were characterized by field emission scanning electron microscopy (FESEM), transmission electron microscopy (TEM), elemental analysis, nitrogen and carbon dioxide adsorption–desorption analysis, X-ray diffraction (XRD), Fourier transform infrared (FTIR), X-ray photoelectron spectroscopy (XPS) and point of zero charge determination. In addition, the equilibrium adsorption data of pure components for all adsorbents were measured at 0, 25 and 50 °C between 0 and 760 mmHg and CO_2/N_2 selectivity was determined. Activated carbons were found to have higher CO_2 adsorption capacity but with a reduction in apparent selectivity. Dynamic binary adsorption simulations performed in a fixed-bed column demonstrated that the activated carbon produced from olive stones with a carbon/KOH ratio of 1:4 (w/w) can separate a mixture of 14 % CO_2 and 86 % N_2 at 25 and 50 °C with the highest selectivity, CO_2 adsorption capacity, CO_2 purity and N_2 recovery factor. Reducing flow rate, the breakthrough time increased. Moreover, the breakthrough time was reduced by increasing the temperature from 25 to 50 °C owing to the exothermic nature of adsorption process.

1. Introduction

The burning of fossil fuels releases greenhouse gases, especially carbon dioxide (CO_2), into the atmosphere, which contributes to global warming and climate change [1–3]. Therefore, it is necessary to develop technologies at the industrial level for CO_2 capture for utilization and storage (CCUS) to drastically reduce greenhouse gas emissions and protect the environment [4–8]. There are variety of strategies to reduce the amount of CO_2 emissions in the atmosphere, including: a) Substituting fossil fuels for sustainable energy sources like wind, solar, biomass, and geothermal, b) enhancing fuel energy efficiency, c) cutting down on the need for energy, d) changing technologies to utilize low-carbon energy sources like natural gas, and e) pre-, post-, and oxy-combustion CO_2 capture scenarios [9,10]. Post-combustion CO_2 capture, which is used to retrofit both newly designed and existing facilities and units and is extensively considered as a durable option to reduce CO_2 emissions quickly and noticeably in the mid-term, allows CO_2 to be separated from flue gas streams produced by large stationary sources, such as fossil fuel-based power plants, cement kilns, steel or iron industries, and oil refineries, after combustion. The collected CO_2 can either be stored in abandoned or depleted oil and gas reservoirs to be used in miscible and immiscible CO_2 floodings for enhanced oil recovery (EOR) procedures or in deep ocean locations [11–13] or be used as an advantageous feedstock to convert into useful chemicals and fuels [14–16]. The principal difficulties of CO_2 capture under post-combustion conditions are the low partial pressure of CO_2 (0.03–0.2 bar) and then the low CO_2 concentration (4–15 %) in the flue gas, which weaken the driving force for CO_2 [17–21].

In recent years, chemical absorption-based aqueous amine scrubbing has been commonly applied for post-combustion CO_2 capture in a large

* Corresponding author.
E-mail address: julia.gonzalez@usc.es (J. González-Álvarez).

https://doi.org/10.1016/j.seppur.2024.127110
Received 1 December 2023; Received in revised form 28 February 2024; Accepted 12 March 2024
Available online 16 March 2024

scale using monoethanolamine (MEA), diethanolamine (DEA), and methyldiethanolamine (MDEA) solutions [22–24]. However, despite its high effectiveness in capturing CO_2, this process requires a significant amount of energy to regenerate the absorbent and recover CO_2, and this energy penalty can raise both capital and operating expenses. Moreover, the corrosive nature of amine solutions and the amine loss experienced throughout the operation owing to evaporation and degradation are two significant flaws of this process that create environmental issues and restrict its widespread application [25]. Adsorption process offers a viable substitute for the aqueous amine scrubbing technique with the ability to minimize the amount of energy needed for regeneration and boost the capacity and selectivity towards CO_2 based on the development of adsorbents [12,26–28].

Carbon-based adsorbents fabricated from biomass precursors are attractive for post-combustion CO_2 capture by adsorption due to widespread availability, low cost and the probability of reaching high CO_2 uptake and selectivity [29]. Furthermore, carbon materials show high surface area and pore volume, particularly micropores, and, as a result, have a high capacity for CO_2 adsorption [30,31]. In comparison to zeolites and metal–organic framework materials (MOFs), carbon adsorbents are easily regenerable, and they are also hydrophobic and possess high stability in the presence of water [32]. These characteristics and the possibility of carrying out modifications in the porous structure (by physical and chemical methods) allow to improve the separation degree [33,34].

Typically, carbon adsorbents fabricated from biomass precursors fall into one of two categories: i) Only carbonization, and ii) carbonization followed by physical or chemical activation. Physical activation involves carbonizing biomass first and then activating them employing oxidizing gases such as CO_2, air and steam, whereas in chemical activation carbonaceous materials are impregnated with chemical agents such as KOH, NaOH, $ZnCl_2$, and $FeCl_3$. The great micropore volume and large surface area are the key benefits of chemical activation over physical activation. So far, some studies have been performed on the preparation of activated carbons fabricated from biomass resources such as olive stones and almond shells using a physical activation, especially with CO_2, and investigation of their performance on CO_2 selectivity under post-combustion conditions [35–38]. However, a review of the literature demonstrates that no studies have been conducted on the fabrication of chemically activated carbon adsorbents using these renewable biomass precursors to investigate how an activating agent affects the selectivity of CO_2 over N_2 in a post-combustion stream.

Therefore, in this work, carbon-based adsorbents fabricated from olive stones and almond shells including carbonized and chemically activated carbons using potassium hydroxide (KOH) with different carbon/KOH ratios were applied to evaluate their performance on the CO_2/N_2 selectivity and the adsorption capacity of CO_2 under post-combustion conditions. Moreover, the impact of feed stream temperature and flow rate on the selectivity and adsorption capacity towards CO_2 was assessed using binary dynamic adsorption simulations in Aspen Adsorption V10 by analyzing the breakthrough curves, N_2 recovery factor and purity of gases. The multi-component adsorption equilibrium has also been predicted using the isotherm experimental data of pure components and the ideal adsorption solution theory (IAST). In addition, this work is focused on the combination of experimental adsorption equilibrium data corresponding to pure gases and a commercial simulation tool that allows to take a step further on screening and analysis of adsorbents for their use in industrial processes evaluating equilibrium and mass transfer characteristics.

2. Materials and methods

2.1. Materials

Olive stones and almond shells supplied by Fertínez Company (Jaén, Spain) and Biogramasa Company (Granada, Spain), respectively, were used as precursors for the carbons fabricated in the present research work. Both raw materials were previously milled and sieved, and the particles with size lower than 3 (for olive stones) and 5 mm (for almond shells) were used for further treatment.

Potassium hydroxide (KOH 85 %, Probus) was employed as activating agent. Hydrochloric acid (HCl 37 %, Sigma Aldrich) and sodium hydroxide (NaOH 98 %, Sigma Aldrich) were used to remove the excess of potassium hydroxide after activation and for the point of zero charge determination.

2.2. Carbon fabrication procedure

Six carbons have been fabricated using almond shells (A) and olive stones (O) under the different conditions shown in Table 1. The precursors (30 g of olive stones and 25 g of almond shells, approximately) employed to produce the adsorbents were carbonized at 600 °C for 1 h under nitrogen atmosphere (34 L h^{-1}) in an oven (Nabertherm GmbH-Germany) and using a temperature ramp of 5 °C min^{-1} up to target temperature. An initial inertization step with the same nitrogen flow rate was carried out for 30 min.

Activation procedure consisted of a mixing step by milling the carbon with different amounts of KOH to reach carbon/KOH ratios of 1:2 and 1:4 (w/w). Then, these mixtures were activated in the oven using a procedure similar to that for the carbonization step but at 850 °C for 2 h. The same temperature ramp (5 °C min^{-1}) and nitrogen flow rate (34 L h^{-1}) were used. After cooling down, the materials were washed with HCl aqueous solutions (0.1 M), followed by double distilled water until constant pH were reached. The activated carbons were then dried overnight at 105 °C. This procedure was based on previous works [39] selecting a temperature of 850 °C as it maximized surface area maintaining a high microporosity degree.

The overall yield of carbons was calculated using Eq. (1):

$$Y(\%) = \left[\frac{m_{c,final}}{m_{b,initial}}\right] \times 100 \quad (1)$$

where Y refers to the overall yield of carbon obtained, and $m_{c,\ final}$ and $m_{b,\ initial}$ are the final mass of carbon after washing and drying (g) and the initial mass of biomass precursor (g) on dry basis, respectively.

2.3. Adsorbent characterization

The adsorbents employed in the present work have been characterized using different techniques that allow to analyze experimental gas adsorption data. Surface textural properties (mainly surface area and pore volume) were obtained using an ASAP 2020 sorption analyzer (Micromeritics). Nitrogen adsorption and desorption data at −196.15 °C and carbon dioxide adsorption data at 0 °C were used to obtain information for this type of characterization. Samples were outgassed under vacuum at 300 °C using a temperature ramp of 10 °C min^{-1} for 2 h that allowed to reach a suitable degas operation. BET equation was used to determine surface area using both CO_2 and N_2 adsorption data which

Table 1
Carbons fabricated from biomass precursors for CO_2/N_2 separation using adsorption.

Carbon	Conditions
OC	Non-activated
OAC1	Carbon/KOH = 1:4 (w/w)
OAC2	Carbon/KOH = 1:2 (w/w)
AC	Non-activated
AAC1	Carbon/KOH = 1:4 (w/w)
AAC2	Carbon/KOH = 1:2 (w/w)

OC: olive stones carbon; OAC: olive stones activated carbon; AC: almond shells carbon; AAC: almond shells activated carbon

were carried out in duplicate. Total pore volume was determined using the amount of nitrogen adsorbed at a relative pressure of 0.99. Micropore (<2 nm) volume was obtained by the difference between the total meso (2–50 nm) and macropore (>50 nm) volumes. Moreover, the two-dimensional non-local density functional theory (2D-NLDFT) model was used to determine pore size distribution of the carbons from simultaneous analysis of both CO_2 and N_2 adsorption data.

Point of zero charge (pH_{pzc}) of the materials was determined as proposed by Carabineiro et al. [40]. Several flasks were filled with aqueous solutions (10 mL) of 0.01 M NaCl at different pH values (between 2 and 12) by adding different amounts of NaOH and HCl solutions (0.1–2 M). Once pH was adjusted, the material was added (10 mg) to each flask and shaken at 350 rpm and 25 °C using an orbital shaker for 48 h to reach adsorption equilibrium. After this period, the final pH was measured and the point of zero charge was determined as the crossing point of the curve generated by the final and initial pH data, with the line corresponding to initial pH = final pH.

The morphological and structural features of the different carbons were obtained by using field emission scanning electron microscopy (FESEM) and transmission electron microscopy (TEM). TEM analysis was performed using a transmission electron microscope (JEOL JEM 2010) operating at 200 keV. To carry out TEM measurements, the samples were homogenized in ethanol using sonication, placed on a 400 mesh copper TEM grid covered with a thin layer of amorphous carbon, and then dried in the air. The surface chemical composition analysis was performed using a Zeiss Fesem Ultra Plus with EDX. Moreover, a CHNS elemental analyzer (Thermo Scientific) was used to determine the content of carbon (C), hydrogen (H), nitrogen (N), sulfur (S) and oxygen (O) (by difference).

X-ray diffraction (XRD) analysis was carried out to investigate the crystalline structure of the carbons using a X-ray diffractometer (Bruker D8 Advance) in Bragg-Brentano geometry. The XRD instrument was equipped with a Cu x-ray tube sealed (CuKα1, λ = 1.5406 Å) and a LYNXEYE XE-T type detector, operating at 40 kV and 40 mA in theta/theta configuration. The diffractograms were generated within the angular range of $3 < 2\Theta < 75^{\circ}$ with a 0.02° step at 2 s per step. The software used in the mathematical analysis of the diffractograms was PANAlytical-HighScore-Plus.

The surface functional groups of the carbons were identified using Fourier transform infrared (FTIR) spectra (VARIAN FTIR 670 spectrometer) and X-ray photoelectron spectroscopy (XPS) (Thermo Scientific NEXSA). For FTIR analysis, sample pellets were prepared by grounding 0.4 mg of carbon with 600 mg of potassium bromide salt (KBr). The spectra were obtained over the wave number range of 400–4000 cm^{-1}. Regarding the XPS technique which is also used to determine the surface elemental composition of the carbons, the instrument was outfitted with a 1486.6 eV X-ray source using aluminum Kα monochromatized radiation. Photoelectrons were gathered at a 90° take-off angle relative to the surface of the sample. The analysis was conducted in a Constant Analyzer Energy mode (CAE), employing a pass energy of 100 eV for survey spectra and 20 eV for high-resolution spectra. Charge referencing was achieved by aligning the lower binding energy C1s photo peak at 284.80 eV, corresponding to the C1s hydrocarbon peak. The surface elemental composition of the carbons was identified by employing the established photoemission cross sections developed by Scofield.

The solid density of carbons was determined by helium pycnometry using an Accupyc II 1345 apparatus (Micromeritics), being the average value of 10 measurements. Before analysis, the different samples were dried at 105 °C for 24 h.

2.4. Pure components adsorption isotherms

The evaluation of gas separation characteristics of the carbons was carried out on the basis of pure gas (CO_2 and N_2) adsorption isotherms at different temperatures. To obtain these data, the static volumetric apparatus (ASAP 2020 analyzer, Micromeritics) has been employed. A suitable degasification step (previously described in section 2.3) was carried out before adsorption experiments. CO_2 and N_2 adsorption isotherms were determined at different pressures (0–760 mmHg) and temperatures (0–50 °C). Experiments at 0 °C were carried out using an ice-bath in a Dewar, and a water bath and a temperature controller (Selecta Sensoterm) were employed to perform experiments at the other temperatures. All the experiments were conducted in duplicate.

The evaluation of models for fitting experimental data has a high importance to be employed in other types of calculations and simulations. In the present work, an appropriate fitting of adsorption isotherms has a high interest to reach suitable simulation results for steady state CO_2 separation by fixed-bed adsorption. For this purpose, the experimental data corresponding to the adsorption isotherms of pure CO_2 and N_2 obtained at 0 °C, 25 °C, and 50 °C between 0 and 760 mmHg for all the adsorbents were fitted using three well-known isotherm models, Langmuir, Freundlich, and Langmuir-Freundlich (Sips) equations, as shown in Table 2.

The non-linear regression analysis in the Microsoft Excel Solver tool was performed to determine the isotherm parameters of CO_2 and N_2 ($q_{m,i}$, b_i, $k_{f,i}$, $n_{f,i}$ *and* $n_{s,i}$) by minimizing the sum of squared residuals (SSR) between the experimental and predicted data:

$$SSR = \sum_{1}^{N} \left(q_{i,exp} - q_{i,model}\right)^2 \tag{5}$$

where $q_{i,\mathrm{exp}}$ and $q_{i,model}$ are the amounts of adsorbed gas experimentally and predicted by the model, respectively, and N is the total number of experimental data.

The coefficient of determination (R^2) and the mean relative absolute deviation (MRAD) were considered as goodness of fit measures to assess how well the data matched the regression model:

$$SST = \sum_{1}^{N} \left(q_{i,exp} - \bar{q}_{i,exp}\right)^2 \tag{6}$$

$$R^2 = 1 - \frac{SSR}{SST} \tag{7}$$

$$MRAD = \frac{1}{N}\sum_{1}^{N}\left[\frac{\left|q_{i,exp} - q_{i,model}\right|}{q_{i,exp}} \times 100\%\right] \tag{8}$$

where SST is the total sum of squares, and $\bar{q}_{i,exp}$ is the mean of the experimental data, which is defined as $\bar{q}_{i,exp} = \frac{1}{N}\sum_{1}^{N} q_{i,exp}$.

2.5. Kinetic experiments and CO_2 mass transfer coefficient determination

Describing the adsorption kinetics has great importance for the simulation of gas separation processes. In this work, the linear and quadratic driving force models (Eqs. (9) and (10)) were used to fit the experimental data obtained for the adsorption kinetics of CO_2 at 25 °C

Table 2
Adsorption isotherm equations used to model the equilibrium data of pure components.

Langmuir	$q_i = q_{m,i}\frac{b_i P_i}{1 \pm b_i P_i}$	(2)
Freundlich	$q_i = k_{f,i} P_i^{1/n_{f,i}}$	(3)
Langmuir-Freundlich (Sips)	$q_i = q_{m,i}\frac{(b_i P_i)^{1/n_{s,i}}}{\left[1 + (b_i P_i)^{1/n_{s,i}}\right]}$	(4)

q_i, the amount adsorbed of component i (kmol kg^{-1}) under equilibrium temperature (T) and pressure (P), $q_{m,i}$ is the maximum amount adsorbed of component i (kmol kg^{-1}), b_i is the affinity constant (bar^{-1}), $k_{f,i}$ is the Freundlich constant (kmol bar^n kg^{-1}), and $n_{f,i}$ *and* $n_{s,i}$ are variables that describe the system's heterogeneity between component i and the surface of the adsorbent.

and 50 °C, and a pressure of 0.8 bar to determine the CO_2 mass transfer coefficients corresponding to the carbons.

$$\frac{\partial q_{CO_2}}{\partial t} = k_{CO_2}\left(q_{e,CO_2} - q_{CO_2}\right) \quad (9)$$

$$\frac{\partial q_{CO_2}}{\partial t} = k_{CO_2}\left(\frac{q_{e,CO_2}^2 - q_{CO_2}^2}{2q_{CO_2}}\right) \quad (10)$$

where q_{e,CO_2} and q_{CO_2} are the amount adsorbed of CO_2 (kmol kg^{-1}) at equilibrium and a given time, t (s), respectively, and k_{CO_2} is the CO_2 mass transfer coefficient (s^{-1}). The non-linear regression analysis described in section 2.4 was used to determine the CO_2 kinetic parameters (q_{e,CO_2} and k_{CO_2}).

The experimental data were obtained using Rubotherm Metal magnetic suspension balance with a resolution of 10 μg and outfitted with jacketed chamber thermostated by water circulating from a Huber Ministat 230 thermostatic bath that provided temperature control with a 0.5 °C degree of uncertainty. For each experiment, the sample bucket was initially filled with approximately 1–1.5 g of adsorbent before being positioned inside the measurement chamber. After the chamber has been vacuumed and fluxed with helium gas (Nippon Gases, Spain, 99.999 %) several times, it was allowed to degas the sample by conditioning it under vacuum (absolute pressure less than 0.05 bar) for at least 6 h at roughly 70 °C.

2.6. Fixed-column dynamic adsorption simulations

A simulation process using a fixed-bed column adsorption model in Aspen Adsorption V10 was applied to evaluate the CO_2 adsorption capacity under post-combustion conditions of carbon-based adsorbents fabricated from olive stones and almond shells. The column used in the dynamic simulations with an inner diameter of 1.86 cm and an effective height of 13 cm (based on a glass laboratory column) was fed with a mixture of 14 % CO_2 and 86 % N_2. Breakthrough curves were simulated at atmospheric pressure and temperatures of 25 °C and 50 °C and different flow rates of 60, 120, 180 and 240 sccm (standard $cm^3\ min^{-1}$) under the following assumptions:

a) The Peng-Robinson equation of state was used as a viable thermodynamic model to describe the behavior of gases.

b) The Upwind Differencing Scheme 1 (UDS1) was used to discretize partial differential equations (PDEs) due to its relatively high accuracy and low computation time for dynamic simulations.

c) The pressure drop along the column was calculated based on the Ergun equation which is applicable to both laminar and turbulent flows.

d) Owing to the low dimensions of the column, the radial mixing and axial dispersion were considered negligible to be modeled as a system in plug flow.

e) The extended model of Langmuir equation and Ideal Adsorbed Solution (IAS) theory were used to estimate the equilibrium of competitive adsorption after identifying the best isotherm models for each adsorbent.

f) The kinetics and mass transfer of the gases were predicted using the lumped resistance and quadratic driving force models.

g) It was assumed that the adsorption column functions under isothermal conditions so that the temperature of the gases and solid were kept constant and equal during the experiment.

h) The column porosity was considered constant throughout the column, and the adsorbent particles were supposed to be uniformly shaped as spheres.

3. Results and discussion

3.1. Characterization of carbons

The carbons prepared from olive stones and almond shells have been characterized with various analytical techniques. The overall yield of these porous carbons varied from 16.4 to 28.4 % and from 4.5 to 14.7 % for olive stones and almond shells precursors, respectively, depending on the preparation conditions (Table S1). The significantly lower yield of carbons fabricated from almond shells compared to those of olive stone-based carbons could be related to differences in the chemical composition of precursors [41]. Figs. 1 and 2 show some SEM images for the activated and non-activated carbons. For both precursors, the non-activated carbons show an important presence of micropores in the external surface. The activation process with different amounts of KOH causes certain modifications in the material surface and in the small-size pores. Thus, porous structure seems more irregular, but the activated carbons maintain an important presence of pores in the range of microporosity.

SEM characterization was completed with EDX analysis, and the data are shown in Table 3 to analyze the surface chemistry. The experimental data indicated relatively similar characteristics of carbons from both precursors. The activation process with a carbon/KOH ratio of 1:2 produced small changes with a slight decrease in the percentage of carbon by an increase in oxygen (AAC2) and potassium (OAC2 and AAC2). When the activation treatment is carried out with a high carbon/KOH ratio (1:4), a higher decrease in the percentage of carbon with an important increase in potassium was observed.

Moreover, TEM analysis was carried out to reveal the morphological structure of carbon materials, as it can offer additional insights into micropores and the results obtained are displayed in Fig. 3. As seen, wormhole-like micropores are dispersed randomly throughout the carbon's framework, which is attributed to the stacking of graphene layers [42], evidencing a substantial presence of microporosity. This distribution of micropores with no discernible pattern could be related to the amorphous nature of these carbons [42] as deduced from the XRD results (Fig. 4). Non-activated carbons (Fig. 3A and D) exhibit a higher degree of organization compared to activated carbons (Fig. 3B, C, E and F). As activation occurs, there is a rise in the disordering of carbon structure causing a decrease in the observed structural organization. Thus, the morphology and structure of these carbons improved, which is consistent with SEM analysis. These findings are in agreement with the results of Lillo- Ródenas et al. [43], that suggested that activation is associated with a reaction involving carbon and potassium hydroxide.

The phase and crystalline structure of the carbons was analyzed from XRD diffractograms, which are illustrated in Fig. 4. Two basic contributions are observed from the diffractograms obtained for non-activated carbons (Fig. 4A): a) Two broad bands at roughly 23° and 43° due to the presence of poorly crystalline phases [44] that confirm the presence of the (0 0 2) and (1 0 0) crystal planes in carbon materials, respectively, b) The appearance of narrow peaks that are assigned to phases with a higher degree of crystallinity. However, in the case of activated carbons (Fig. 4B), the diffractograms obtained show a small amount of amorphous components with a low degree of graphitization. It can be due to the KOH activation at high temperature that destroys the atomic arrangement of the carbons [39].

Elemental analysis was also performed to evaluate the content of C, H, N, S and O in carbons and the results obtained are given in Table 4. As seen, after the activation treatment, the oxygen content of OAC1 and OAC2 increased from 13.75 % to 35.08 % and 33.00 %, respectively, compared to OC, and from 14.42 % to 18.96 % and 31.90 % for AAC1 and AAC2 compared to AC, respectively. The activated carbon produced from olive stones with a carbon/KOH ratio of 1:4 (OAC1) was found to have the highest oxygen content, which can confirm the presence of more oxygen-containing functional groups on the surface of the carbon in comparison to the other activated carbons.

FTIR analysis was carried out to assess the surface chemistry of the carbons and the corresponding spectra are presented in Fig. S1. As seen, the strong band observed at 1099 cm^{-1} could be contributed to C-O stretching of ether and alcohol which indicates the presence of hydroxyl functional groups. The peaks at 472 and 796 cm^{-1} show the generation

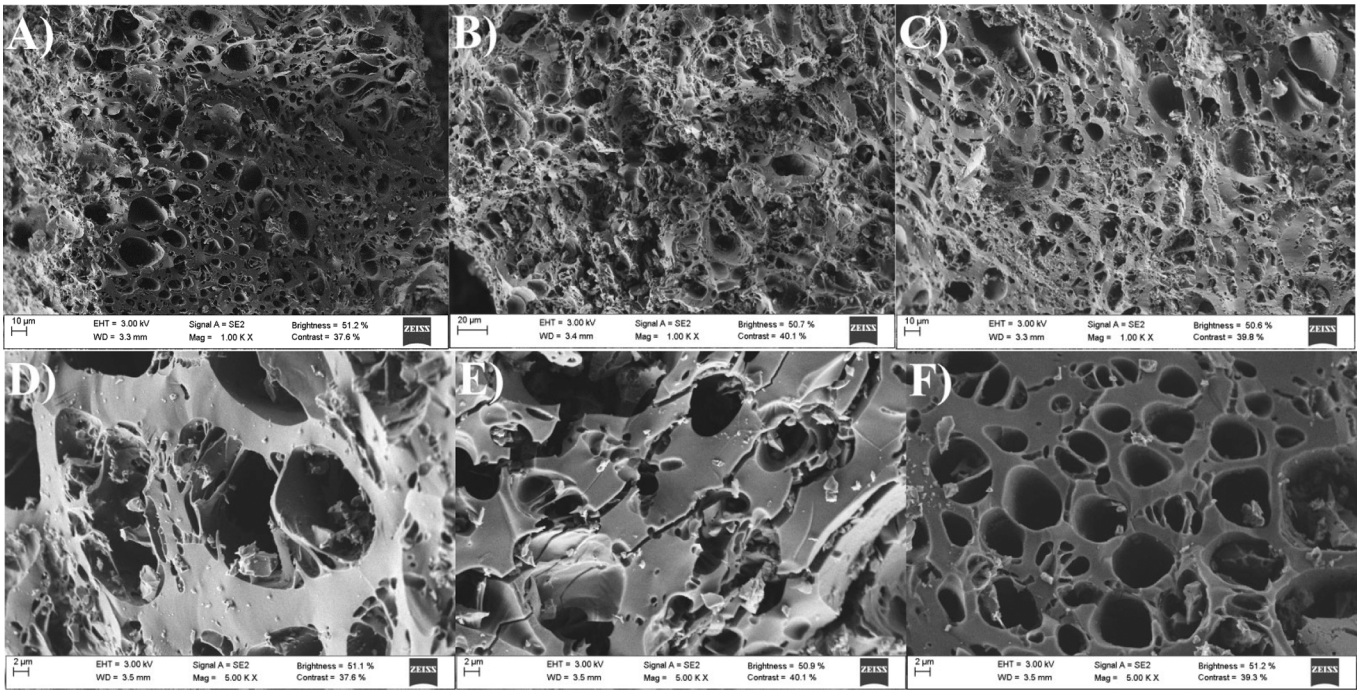

Fig. 1. SEM images of adsorbents fabricated from olive stones with different magnifications: A)- OC × 1000 B)- OAC1 × 1000 C)- OAC2 × 1000 D)- OC × 5000 E)- OAC1 × 5000 F)- OAC2 × 5000.

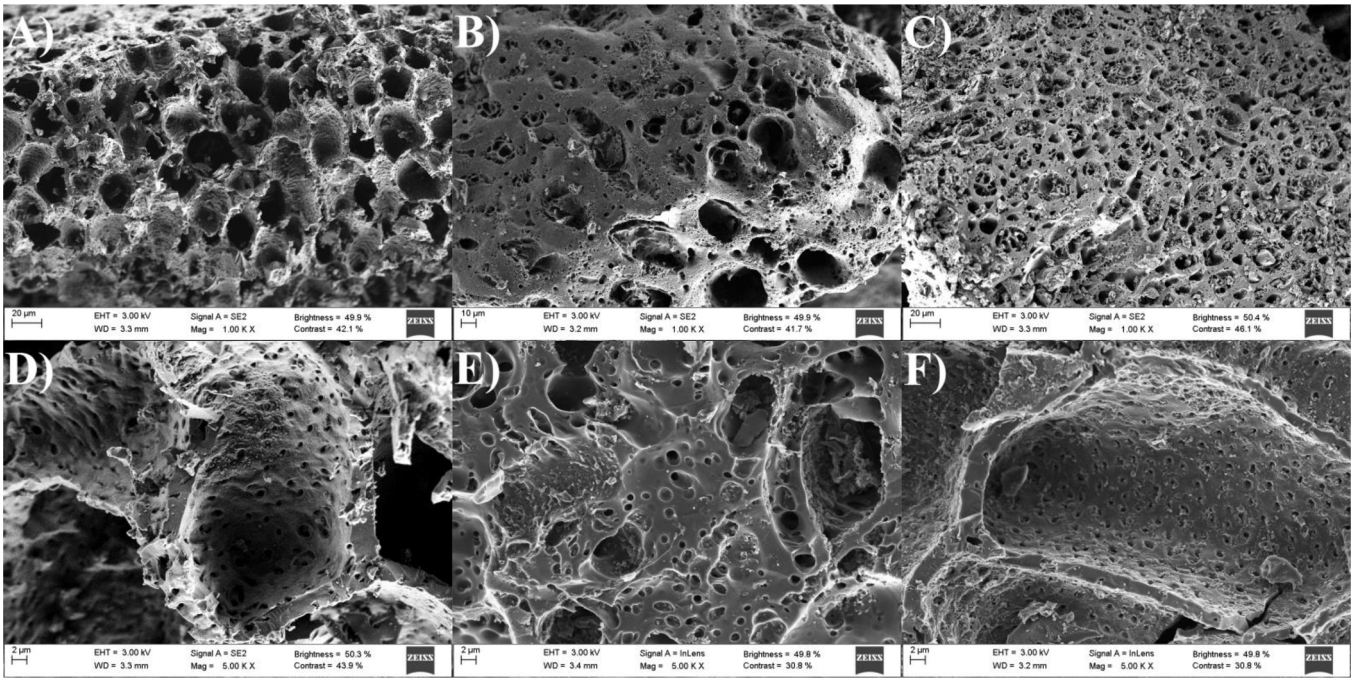

Fig. 2. SEM images of adsorbents fabricated from almond shells with different magnifications: A)- AC × 1000 B)- AAC1 × 1000 C)- AAC2 × 1000 D)- AC × 5000 E)- AAC1 × 5000 F)- AAC2 × 5000.

of C–H groups and the peak at 1400 cm^{-1} can be assigned to C-N stretching. A weak peak was observed at 1726 cm^{-1} confirming the presence of carboxylic and carbonyl groups (C = O stretching). Moreover, the peaks at 2850 and 2920 cm^{-1} may be due to stretching vibrations in C–H and N–H bonds and the peak at 3419 cm^{-1} corresponds to the existence of hydroxyl (–OH stretching) and amine groups (–NH stretching).

The survey XPS spectra have allowed to determine the surface elemental composition analysis of the carbons, and the results are depicted in Fig. S2. As observed earlier, C and O emerge as the primary constituents, corroborated by the presence of C1s and O1s peaks (Fig. S2) at 285–287 and 532.5 eV, respectively. A weak peak observed at around 399.8–400 eV is attributed to N1s photoelectrons, indicating a very low amount of nitrogen in nearly all the carbons. These findings align with the results obtained from elemental analysis (Table 4).

To analyze the surface chemical state of carbons using XPS

Table 3
Surface chemical composition of the carbons (C) and activated carbons (AC) fabricated from olive stones (O) and almond shells (A) using EDX analysis.

Carbon	% C	% O	% K	% Ca	% Fe
OC	89.1	9.5	0.7	0.6	–
OAC1	82.8	10.4	4.8	0.2	0.9
OAC2	88.9	8.8	1.4	0.2	0.4
AC	90.8	8.0	0.7	0.4	–
AAC1	91.0	7.2	0.7	0.4	0.4
AAC2	86.8	8.8	3.3	0.7	0.2

technique, C1s, N1s and O1s high-resolution spectra were also obtained and the results are presented in Tables 5 and 6. Five peaks are detected in the C1s spectra (Table 5). The peak at 284.8 eV is associated with the presence of C–C, C=C or C–H bonds and the peak around 286 eV is assigned to C–OH and C–O–C groups [39]. The peaks at about 288 and 289 eV are assigned to carbonyl (C=O) and ester (O–C=O) functional groups, respectively [39]. Finally, a peak was observed at around 290 eV, corresponding to carbonate groups [39], for olive stone activated carbons.

Moreover, in the C1s spectrum of three carbons (OAC1, OAC2 and AAC2), distinct contributions from the spin–orbit splitting of the 2p

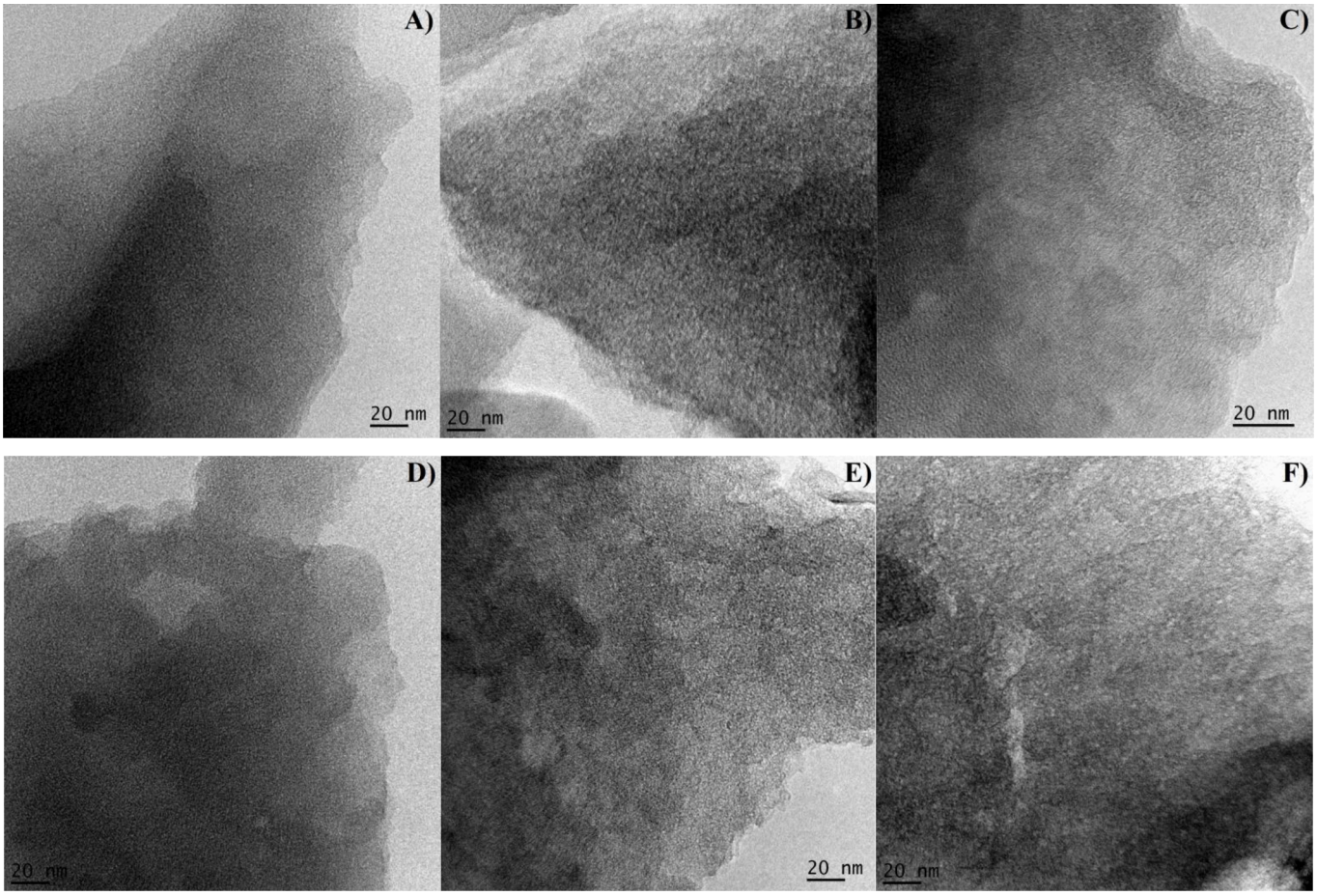

Fig. 3. TEM images of carbons fabricated from olive stones and almond shells: A)- OC B)- OAC1 C)- OAC2 D)- AC E)- AAC1 F)- AAC2.

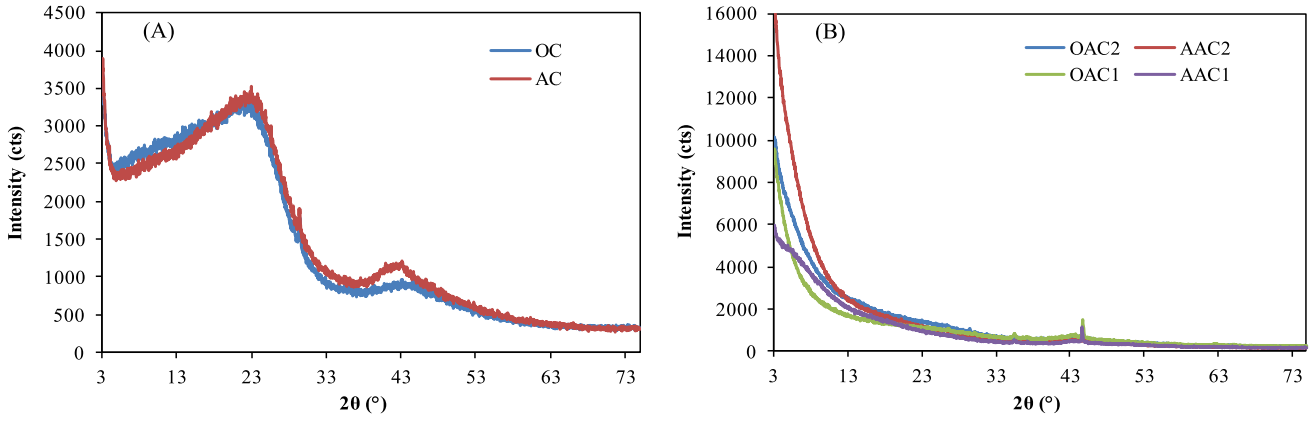

Fig. 4. XRD diffractograms of A)- non-activated carbons and B)- activated carbons fabricated from olive stones (O) and almond shells (A).

Table 4
CHNS elemental analysis of the carbons (C) and activated carbons (AC) fabricated from olive stones (O) and almond shells (A).

Carbon	% C	% H	% N	% O*
OC	83.82	2.21	0.22	13.75
OAC1	62.55	2.20	0.17	35.08
OAC2	64.16	2.56	0.28	33.00
AC	83.42	1.92	0.24	14.42
AAC1	80.24	0.39	0.41	18.96
AAC2	65.22	2.00	0.88	31.90

* Calculated by difference.

orbital, namely K2p3/2 and K2p1/2, were observed (Fig. S3). These contributions suggest that potassium ions may either bind to remaining oxygen atoms or become intercalated within the carbon structure [45]. Concerning the high-resolution spectra of N1s (Table 6), which were fitted for all carbons with the pyrrolic-N groups, it is observed that for OAC1, OAC2 and AAC2 an additional component appeared within the range of 406 to 407 eV, corresponding to -O-NO_2 (nitro-oxy) groups, whose relative percentage increased for olive stone-based carbons as the activation treatment intensifies. Regarding O1s high-resolution spectra (Table 6), which were fitted with two or three components, depending on the carbon, the peaks in binding energy ranging from 531.9 to 532.5 eV are attributed to oxygen in non-carbonyl structures, such as ether formations in esters and anhydrides and the peaks falling within the range of 533.1 to 533.9 eV are associated with oxygen atoms in carboxylic functional groups (–COOH and –COOR) [46]. The amount of oxygen can be a good indicator for assessing the proportion of carbon–oxygen functional groups present on the surface of the samples (Table 5). It is possible to observe that activated carbons (OAC1, OAC2 and AAC2), apart from AAC1, showed significant high oxygen contents, which are in agreement with the results obtained from the elemental analysis (Table 4). XPS analysis revealed the existence of different surface functional groups in the carbons as previously confirmed by FTIR spectra (Fig. S1). The results obtained from O1s spectra (Table 6) also demonstrated that the main oxygen-containing functional groups in olive stone activated carbons (OAC1 and OAC2), non-activated carbons (OC and AC) and AAC1, and AAC2 were carboxyl, ethers and hydroxyl groups, respectively, which can be favorable for CO_2 adsorption [39].

In addition, the point of zero charge (pH_{pzc}) was determined for each material and the results are shown in Table 7. The pH_{pzc} data allowed to know the basic/acidic character of the materials. Considering that basic adsorbents may be suitable for adsorbing acidic gases, the order for basic character is OC ~ AC < AAC1 ~ AAC2 < OAC1 < OAC2. These data allowed to conclude that the activation treatment leads to the production of more alkaline materials than the non-activated ones. This behaviour is probably due to the generation of hydroxyl functional groups in the carbon surface caused by the presence of KOH during activation. Previous studies have concluded that the basic functionalities present in some materials explain their behavior in relation to a higher amount of adsorbed gas [47] as CO_2 is considered as a Lewis acid. In either way, some studies have given a higher importance to other characteristics mainly the pore size distribution upon the amount of CO_2 adsorbed [48,49].

Among the most important studies for solid characterization are the nitrogen adsorption–desorption isotherms that allow to determine surface characteristics and specifically the surface area and pore size distribution. In the present work, gas adsorption isotherms have been determined using N_2 at −196.15 °C (Fig. 5). In addition, the adsorption isotherms of CO_2 at 0 °C were obtained (Fig. 6) to carry out a wider evaluation of surface characteristics of these materials as previous studies recommend [50].

Fig. 5 shows the influence of the treatment carried out for both precursors upon the magnitude and shape of nitrogen adsorption–desorption isotherms. All isotherms (for activated and non-activated materials) show the shape of a type I isotherm that is compatible with materials with a high microporosity. This conclusion is in agreement with the previous observations using the SEM images.

Although all isotherms can be classified as IUPAC type I, for the activated carbons, a slight change in the shape of the isotherm is observed that allows to assign type Ia for the non-activated and type Ib for the activated ones. Isotherms Ib show the presence of the knee in a

Table 7
Point of zero charge of carbons fabricated from biomass precursors.

Carbon	pH_{pzc}
OC	7.7
OAC1	8.8
OAC2	9.4
AC	7.7
AAC1	7.8
AAC2	7.8

Table 5
Components and their relative proportions corresponding to C1s high-resolution spectra (%) for carbons.

Carbon	C–C, C=C, CH_x (284.8 eV)	C–O–C, C–OH (286.1–286.5 eV)	C=O (287.8–288.3 eV)	O=C–O (289 eV)	CO_3 (290.3 eV)	Carbon-Oxygen functional groups
OC	75.39	17.96	3.48	3.17	–	24.61
OAC1	68.29	15.27	8.67	–	7.77	31.71
OAC2	68.24	14.27	9.23	–	8.27	31.77
AC	83.16	11.20	5.65	–	–	16.85
AAC1	83.19	13.22	3.60	7.50	–	16.82
AAC2	70.72	16.00	5.78	–	–	29.28

Table 6
Components and their relative proportions corresponding to N1s and O1s high-resolution spectra for carbons.

Carbon	N1s high-resolution spectra (%)		O1s high-resolution spectra (%)			
	Pyrrolic-N (400–400.5 eV)	-O-N_2 (Nitro-oxy) (406–407 eV)	OH-groups (530.8–531.8 eV)	Organic bonds (531.9–532.5 eV)	Organic bonds (533.1–533.9 eV)	Water adsorbed (534.3 eV)
OC	100.00	–	9.80	48.13	42.07	–
OAC1	37.97	62.03	36.93	–	45.50	17.57
OAC2	65.33	34.67	22.51	34.67	42.82	–
AC	100.00	–	12.06	47.84	40.11	–
AAC1	100.00	–	–	84.15	–	15.85
AAC2	72.96	27.04	69.34	–	30.66	–

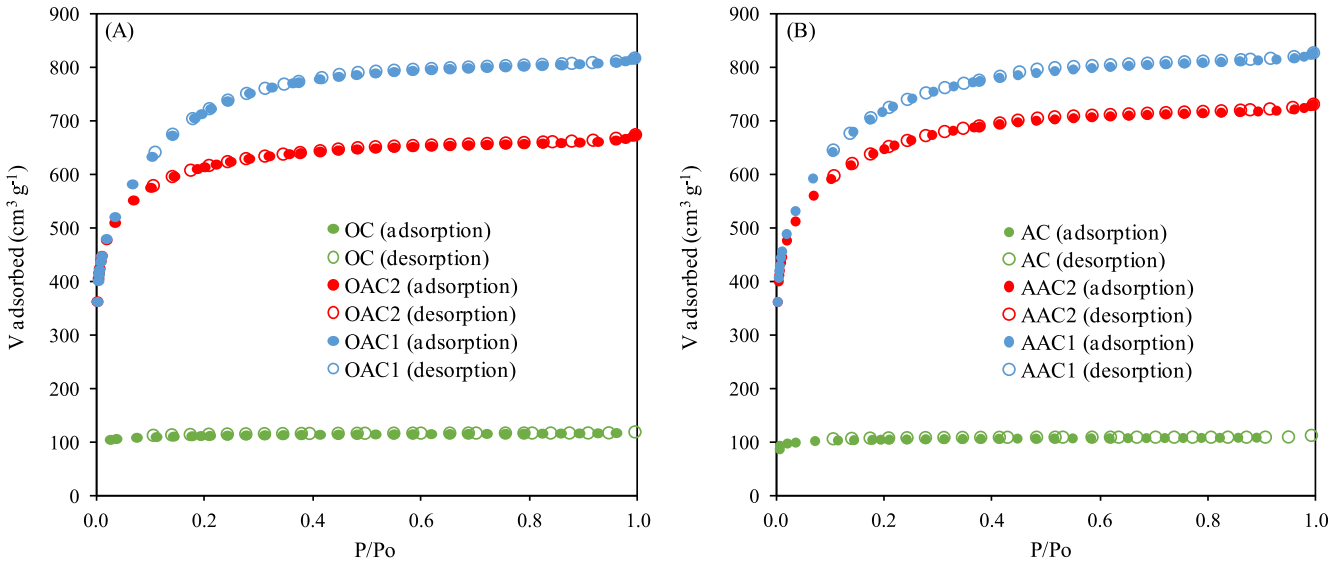

Fig. 5. Nitrogen adsorption–desorption isotherms at −196.15 °C for the carbons prepared from biomass precursors. (A)- Olive stone-based carbons (B)- Almond shell-based carbons.

wider range of relative pressures. This change could be related to (i) an increase in the pore diameter in the microporosity range and/or (ii) the generation of narrow mesopores [51].

Analyzing the magnitude of the amount of nitrogen adsorbed by each material (Fig. 5), an important increase was observed after carbon activation, and especially using the higher carbon/KOH ratio. This behavior is usually attributed to an increase in the specific surface area that is caused by the activation [44] though this conclusion is subsequently confirmed by determining its value using BET equation.

As previously indicated, BET equation has been used to fit the experimental data of nitrogen adsorption and then to determine the specific surface area of each material. Table 8 includes the values determined for the different parameters related to the porous structure of the carbons. In relation to the specific surface area, a clear increase in its value is observed with carbon activation obtaining the highest surface area for a carbon/KOH ratio of 1:4 (w/w). The increase in surface area produced by activation at a ratio of 1:2 (w/w) was very important (411 % for olive stone and 569 % for almond shell), however, increasing the ratio to 1:4 (w/w) did not significantly enhance the generation of surface area (469 % for olive stone and 653 % for almond shell).

These data have been also used to determine other parameters that allow to characterize the materials. The data included in Table 8 corresponding to the pore volume are in agreement with the previous discussion about the shape and classification of nitrogen isotherms. When activation is used, the pore size increases losing microporous structure (% of microporosity). Thus, the non-activated carbons reached a 90 % of the volume generated by the microporosity. On the contrary, the activated carbons showed a decrease in microporosity until values close to 75 % by an increase in pore size, also in agreement with SEM images (Figs. 1 and 2).

The analysis of carbons porous structure has been completed using experimental data corresponding to carbon dioxide adsorption isotherms at 0 °C (Fig. 6). Manyà et al. [52] have analyzed the information obtained with this type of experiments and concluded that it allows to evaluate the surface area generated by the pores with diameters lower than 0.7 nm (ultramicropores). Serafin et al. [53] have concluded that the presence of small pores in the range of ultramicroporosity can increase the amount of CO_2 adsorbed. The calculated data (Table 8) show the high importance of this type of pores (ultramicropores) reaching high surface areas. Activation, especially at high temperature, also causes an increase in both surface area determined with CO_2 and microporosity, increasing the accessibility of gas to the porous structure of materials [54,55]. However, an increase in the carbon/KOH ratio (from 1:2 to 1:4 w/w) used does not enhance the development of ultramicropores. Specifically, for carbons produced from olive stones, an important decrease in surface area for OAC1 was observed. This behavior is explained as previously discussed considering that high KOH dose produces modifications in pores increasing their size and then decreasing the ultramicroporosity.

A more detailed analysis about the porosity of carbons has been carried out based on pore size distribution (PSD), which is shown in Fig. 7. Non-activated carbons produced from both precursors show a PSD centred on ultramicropores range showing two different groups of ultramicropores at 3.6 Å and 5.4 Å, approximately.

Considering the activated materials, almond shell-based carbons show a clear influence of carbon/KOH ratio. Thus, an increase in this ratio causes a decrease in low-size ultramicropores and an increase in the pores with larger diameters. For carbon prepared with 1:2 ratio, an increase in large-size ultramicropores and supramicropores is observed while the use of 1:4 ratio enhances mesopores formation. This behavior agrees with the values of microporosity degree included in Table 8.

In relation to the materials fabricated using olive stones as precursor, the behavior shows that an increase in the amount of KOH causes an enhancement in supramicropores and mesopores as almond shell carbons. However, a difference was found in the analysis of ultramicropores. For this size range, an increase in carbon/KOH ratio caused an increase in the low-size ultramicropores ($D_p < 4.5$ Å) and a decrease in large-size ultramicropores (4.5 Å < D_p < 7 Å).

3.2. *Pure components adsorption isotherms*

The evaluation of the carbons prepared in relation to their use in gas separation process for post-combustion streams was initially performed using the experimental data of pure components adsorption isotherms. The influence of pressure and temperature on the amount of CO_2 and N_2 adsorbed was determined. Fig. 6 shows the adsorption isotherms obtained for pure CO_2 and N_2 at 0 °C, 25 °C, and 50 °C using the different carbons fabricated from almond shells and olive stones as precursors.

As it is observed in Fig. 6, the shape of the CO_2 adsorption isotherms is different for non-activated materials in comparison with the activated ones, which could be indicative of the effect caused by the activation procedure on CO_2 adsorption. When pressure increases, the isotherms

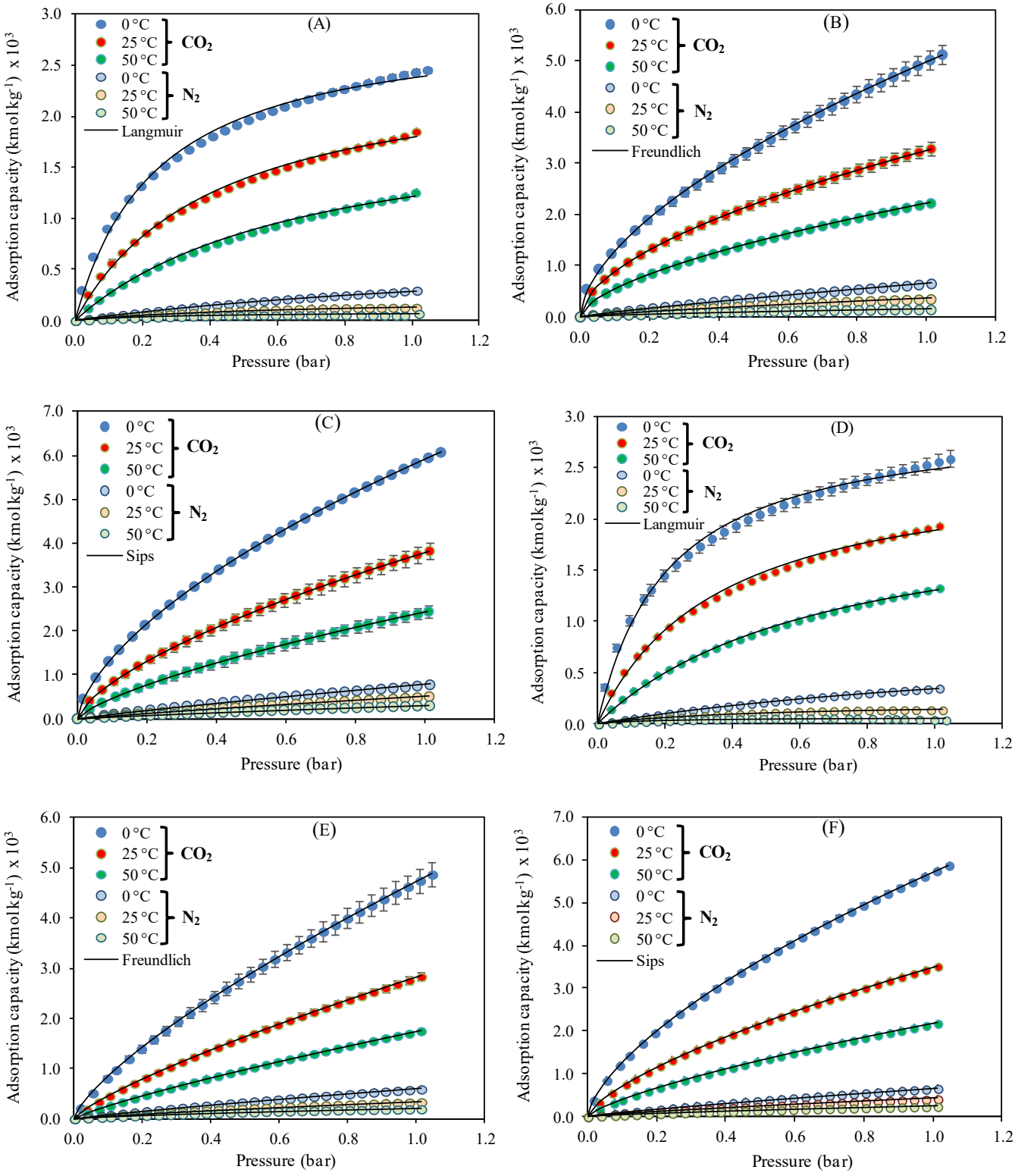

Fig. 6. Experimental and calculated equilibrium adsorption isotherms of pure CO_2 and N_2 corresponding to (A)- OC, (B)- OAC1, (C)- OAC2, (D)- AC, (E)-AAC1, (F)-AAC2 at 0 °C, 25 °C, and 50 °C.

for non-activated carbons tend to reach a relatively constant value. On the contrary, the behavior for CO_2 adsorption using activated carbons shows a continuous increase in the adsorbed amount of this gas. Furthermore, the carbon dioxide adsorption isotherm for AC carbon (Fig. 6D) shows that the amounts of adsorbed carbon dioxide at pressure lower than 0.15 bar are higher than expected in comparison to those for the activated carbons (Fig. 6E and F), being almost of the same order for OC carbon. However, this behavior is opposite at atmospheric pressure. The activated carbon produced from olive stones with a carbon/KOH ratio of 1:2 w/w (OAC2) demonstrates the highest CO_2 adsorption

Table 8
Textural characteristics of the carbons prepared from biomass precursors.

Carbon	S_{BET} [a] (m^2 g^{-1})	S_{BET} [b] (m^2 g^{-1})	V_{total} [c] (cm^3 g^{-1})	V_{meso} (cm^3 g^{-1})	V_{micro} (cm^3 g^{-1})	microporosity (%)
OC	450.2	296.6	0.1836	0.0186	0.165	89.9
OAC2	2302.7	1013.0	1.0394	0.1634	0.876	84.3
OAC1	2561.3	814.5	1.2630	0.3144	0.949	75.1
AC	339.7	300.5	0.1720	0.0170	0.155	90.0
AAC2	2271.6	1016.7	1.1280	0.2440	0.884	78.4
AAC1	2556.7	1090.5	1.2770	0.3250	0.952	74.5

[a] Determined at −196.15 °C with N_2; [b] Determined at 0 °C with CO_2; [c] Determined at $P/P_o = 0.99$.

capacity of 6.07, 3.82 and 2.44 mmol g^{-1} at 0 °C, 25 °C and 50 °C, respectively (Fig. 6C), which could be related to its higher microporosity than that for other activated carbons. Table 9 shows CO_2 adsorption capacity of activated carbons derived from biomass precursors at 1 bar as reported in the literature. It is noticeable that the values obtained in the present work are among the greatest for activated carbons fabricated from biomass waste in the conditions studied. Moreover, CO_2-activated carbons fabricated from olive stones and almond shells [38] show less CO_2 adsorption capacity compared to KOH-activated carbons produced in this study (Table 9).

Based on surface areas (see Table 8), this is not the expected behavior because a large surface area tends to increase the possibilities of molecules adsorption. In fact, when pressure increases, the importance of surface area is observed and a clear enhancement in the amount of adsorbed gas is reached. At low pressures, however, the behavior found, especially for almond-shell carbon, can be explained based on the characteristics of both carbons: (i) the absence of activation (therefore, avoiding the use of higher temperatures and presence of KOH) allows to maintain a higher amount of functional groups [63] that can interact with CO_2 molecules enhancing their adsorption; and (ii) the presence of pores with a lower diameter for non-activated carbon permits to stablish a suitable environment for CO_2 adsorption [64]. In this way, at low partial pressures (e.g. post-combustion streams) the non-activated carbons are competitive with activated ones avoiding the cost associated to activation process (mainly the use of chemicals and high temperatures), and, especially, the almond shell-based carbon with higher adsorption in this range of pressures, since at high pressure (in the range studied) the amount of adsorbed CO_2 for both non-activated carbons is similar. More suitable surface chemistry could be produced in the almond shell-based carbons, although the surface area and pore size are similar for both non-activated carbons.

Analyzing the effect of the carbon/KOH ratio, Fig. 6 shows that the use of high ratio causes a decrease in CO_2 adsorption though the surface areas for AAC1 and OAC1 are the highest (Table 8). Activation with a 1:4 (w/w) ratio causes a higher increase in pore size and generates a more homogeneous surface that does not enhance carbon dioxide adsorption, as seen above.

Table 9
CO_2 adsorption capacity of activated carbons produced from biomass precursors at 1 bar.

Precursor	Activating agent	BET surface area (m^2 g^{-1})	CO_2 adsorption capacity (mmol g^{-1})		Reference
			0 °C	25 °C	
Chestnut shell	KOH	1255	5.23	3.57	[44]
Coffee grounds	KOH	840	4.70	3.00	[56]
Palm fruit bunch	KOH	2510	5.23	3.71	[57]
Jujun grass	KOH	2957	–	2.80	[58]
Camellia japonica	KOH	3537	–	2.80	[58]
Waste tobacco	Methanol	1104	3.56	2.69	[59]
Enteromorpha prolifera	KOH	418	2.39	1.40	[60]
Poplar anthers	KOH	3322	–	2.04	[61]
Mesua ferrea L. seed cake	Calcination	184.1	–	2.63	[62]
Pomegranate peels	KOH	585	6.03	4.11	[53]
Carrot peels	KOH	1379	5.64	4.18	[53]
Fern leaves	KOH	1593	4.52	4.12	[53]
Olive stone	CO_2	1113	–	3.00	[38]
Almond shell	CO_2	822	–	2.70	[38]
Olive stone	KOH	2303	6.07	3.82	This work
Almond shell	KOH	2272	5.87	3.51	This work

In relation to activated carbons, both materials reached higher values for CO_2 adsorption than non-activated ones over the entire pressure range. In the case of olive stones activated carbons, these show similar adsorption behavior at pressure lower than 0.3 bar. This trend is different from the previously shown in Fig. 6E and F for carbons from almond shells. This different behavior for olive stone-based activated carbons was also observed in the values of the point of zero charge that were higher for olive stones carbons (see Table 7) suggesting a more basic surface that could enhance CO_2 adsorption at low surface coverage (low relative pressure range).

N_2 adsorption isotherms present a different behavior compared to those for CO_2. Thus, the amount of nitrogen adsorbed in the carbons show a good correlation with the surface area, which is in agreement

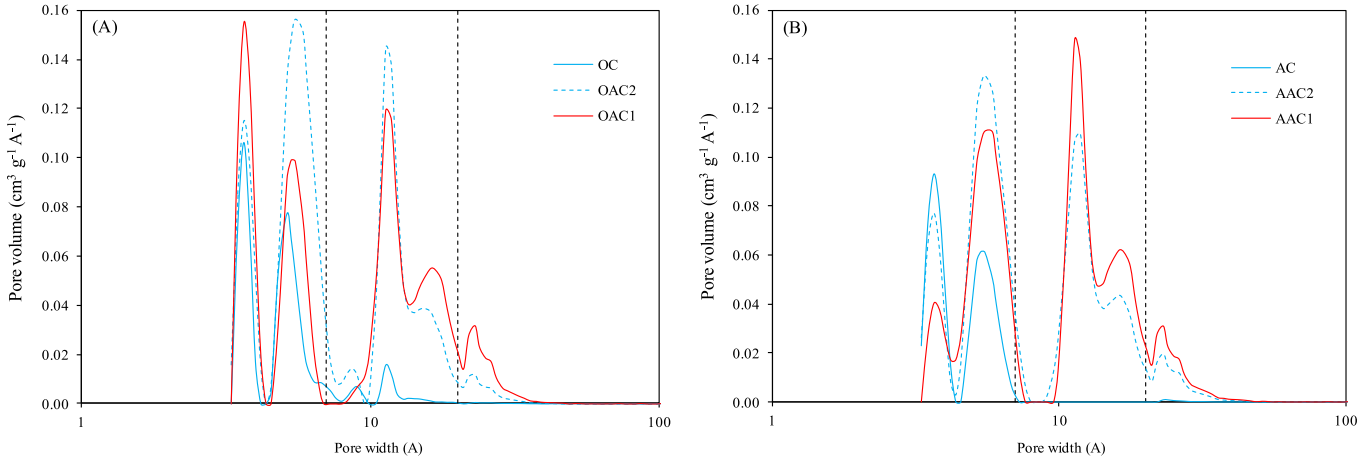

Fig. 7. Pore size distribution of (A)- Olive stone-based carbons (B)- Almond shell-based carbons. Ultramicropores ($D_p < 7$ Å), supramicropores (7 Å $< D_p <$ 20 Å), mesopores (20 Å $< D_p <$ 500 Å).

with a physical adsorption for this gas. The presence or absence of functional groups in the carbon surface does not influence N_2 adsorption. For the activated carbons, nitrogen adsorption shows the same behavior as for carbon dioxide adsorption caused by a higher presence of microporosity in the carbons activated with 1:2 ratio.

Comparing CO_2 and N_2 isotherms using non-activated and activated carbons from both precursors (Fig. 6), it can be observed that the adsorption capacity of CO_2 is considerably higher than that of N_2. This behavior is considered a mandatory characteristic of these materials to be used for gas separation processes under post-combustion conditions.

Even though, as previously commented, the non-activated carbons do not reach CO_2 adsorption values at low pressures like those obtained for the activated carbons, the difference between the adsorbed amounts of CO_2 and N_2 is still high mainly at typical post-combustion CO_2 partial pressures, and for this reason it is important to consider these carbons for further analysis.

The experimental equilibrium data for pure CO_2 and N_2 were fitted to the Langmuir, Freundlich, and Langmuir-Freundlich (Sips) models by performing non-linear regression analysis, and the best-fitting model was selected for each carbon. According to Fig. 6, the isotherm models of Langmuir, Freundlich, and Sips were chosen to describe the adsorption equilibrium between pure components and carbonized olive stones and almond shells (OC and AC), activated olive stones and almond shells carbons with a carbon/KOH ratio of 1:4 w/w (OAC1 and AAC1), and activated carbons with a carbon/KOH ratio of 1:2 w/w (OAC2 and AAC2), respectively.

The corresponding fitting parameters, the coefficient of determination (R^2), and the mean relative absolute deviations (MRAD) for all the carbons at 0 °C, 25 °C, and 50 °C are listed in Table 10. As can be seen from Table 10, R^2 alone is not able to identify the best-fitting models as roughly the same R^2 values were obtained with changing MRAD values. Therefore, both R^2 and MRAD were used to analyze how well the data fit the non-linear regression model. It is worth highlighting that this work is reasonably more focused on fitting the adsorption equilibrium data corresponding to CO_2 due to significantly higher amount of CO_2 adsorbed in comparison with N_2. Table 10 indicates a suitable or good fit for OAC1 (Freundlich equation), OAC2 (Sips equation), and AAC2 (Sips equation) with a MRAD lower than 0.5 %, as well as for AAC1 (Freundlich equation) with a MRAD of approximately 1 % for CO_2 at 25 °C, and 50 °C. Moreover, a reasonable fit was observed for OC and AC using the Langmuir isotherm model with a MRAD below 3.7 % for CO_2.

The parameters n_f and n_s of Freundlich and Sips models provide information about the heterogeneity of carbons surface [65]. Analyzing the values obtained (Table 10), it is possible to observe that for CO_2 adsorption these parameters take the highest values for OC and AC carbons (1.62–2.50 and 1.71–2.70 for n_f and 1.67–2.40 and 1.68–2.62 for n_s, respectively). This fact is in agreement with previous results that concluded a more heterogeneous surface for carbons without activation.

Table 10
Adsorption equilibrium parameters of isotherm models for CO_2 and N_2 on olive stone and almond shell carbons at 0 °C, 25 °C, and 50 °C.

		Langmuir				Freundlich				Sips				
Gas	T (°C)	q_m (kmol kg^{-1})	b (bar^{-1})	R^2 -	MRAD -	k_f (kmol bar^n kg^{-1})	n_f -	R^2 -	MRAD -	q_m (kmol kg^{-1})	b (bar^{-1})	n_s -	R^2 -	MRAD -
OC														
CO_2	0	2.953×10^{-3}	4.136	0.9950	3.54	2.500×10^{-3}	2.50	0.9905	5.03	3.479×10^{-2}	0.0021	2.40	0.9917	4.77
	25	2.535×10^{-3}	2.398	0.9970	2.78	1.870×10^{-3}	2.01	0.9950	3.80	4.354×10^{-2}	0.0019	2.00	0.9955	3.69
	50	2.043×10^{-3}	1.441	0.9983	2.24	1.261×10^{-3}	1.62	0.9974	3.68	2.624×10^{-2}	0.0067	1.67	0.9963	4.67
N_2	0	7.667×10^{-4}	0.600	0.9996	0.72	2.989×10^{-4}	1.25	0.9977	3.77	3.000×10^{-2}	0.0032	1.25	0.9979	3.77
	25	2.292×10^{-4}	1.440	0.9947	3.86	1.400×10^{-4}	1.67	0.9768	10.78	1.975×10^{-2}	0.0009	1.43	0.9661	8.33
	50	7.695×10^{-5}	3.262	0.9491	9.73	6.238×10^{-5}	2.17	0.9010	16.41	2.170×10^{-3}	0.0009	2.00	0.8995	15.17
OAC1														
CO_2	0	8.363×10^{-3}	1.376	0.9879	7.43	4.967×10^{-3}	1.70	0.9997	1.25	8.807×10^{-2}	0.0101	1.64	0.9995	1.61
	25	5.086×10^{-3}	1.620	0.9889	5.90	3.254×10^{-3}	1.77	1.0000	0.23	7.011×10^{-2}	0.0052	1.73	0.9999	0.50
	50	3.582×10^{-3}	1.441	0.9916	5.31	2.205×10^{-3}	1.64	1.0000	0.18	4.694×10^{-2}	0.0077	1.61	0.9999	0.50
N_2	0	2.745×10^{-3}	0.300	0.9999	0.60	6.394×10^{-4}	1.18	0.9994	2.92	3.400×10^{-2}	0.0097	1.17	0.9994	2.90
	25	1.079×10^{-3}	0.470	0.9996	0.73	3.508×10^{-4}	1.25	0.9972	4.45	9.042×10^{-3}	0.0179	1.25	0.9977	4.76
	50	2.860×10^{-3}	1.000	0.9975	2.54	1.487×10^{-4}	1.43	0.9862	7.56	2.840×10^{-2}	0.0006	1.43	0.9864	7.59
OAC2														
CO_2	0	1.063×10^{-2}	1.193	0.9941	6.08	5.925×10^{-3}	1.61	1.0000	0.39	7.401×10^{-2}	0.0240	1.53	1.0000	0.24
	25	7.290×10^{-3}	1.029	0.9955	4.78	3.798×10^{-3}	1.52	1.0000	0.41	7.562×10^{-2}	0.0124	1.48	1.0000	0.05
	50	5.834×10^{-3}	0.700	0.9969	4.60	2.435×10^{-3}	1.41	0.9999	0.51	4.313×10^{-2}	0.0216	1.36	1.0000	0.18
N_2	0	3.283×10^{-3}	0.300	0.9996	1.31	7.677×10^{-4}	1.16	0.9991	2.50	6.890×10^{-2}	0.0062	1.14	0.9988	2.30
	25	2.106×10^{-3}	0.300	0.9996	0.43	4.920×10^{-4}	1.16	0.9994	2.80	5.000×10^{-2}	0.0053	1.14	0.9995	2.22
	50	1.283×10^{-3}	0.300	0.9998	0.80	2.980×10^{-4}	1.19	0.9988	3.71	3.091×10^{-2}	0.0040	1.19	0.9988	3.83
AC														
CO_2	0	3.006×10^{-3}	4.800	0.9933	3.68	2.614×10^{-3}	2.70	0.9905	4.57	5.642×10^{-2}	0.0004	2.62	0.9912	4.39
	25	2.569×10^{-3}	2.747	0.9963	2.95	1.972×10^{-3}	2.12	0.9949	3.47	6.141×10^{-2}	0.0008	2.09	0.9954	3.31
	50	2.206×10^{-3}	1.450	0.9980	2.98	1.346×10^{-3}	1.71	0.9971	3.54	5.373×10^{-2}	0.0021	1.68	0.9974	3.39
N_2	0	9.267×10^{-4}	0.600	1.0000	0.23	3.597×10^{-4}	1.25	0.9964	3.75	3.977×10^{-2}	0.0028	1.25	0.9967	3.70
	25	2.150×10^{-4}	2.000	0.9908	6.00	1.467×10^{-4}	2.00	0.9610	15.21	1.700×10^{-2}	0.0004	1.67	0.9675	10.51
	50	6.800×10^{-5}	5.000	0.8442	14.36	6.272×10^{-5}	2.00	0.6550	19.39	8.011×10^{-3}	0.00006	2.00	0.6554	19.28
AAC1														
CO_2	0	1.209×10^{-2}	0.626	0.9981	4.47	4.728×10^{-3}	1.35	0.9999	0.84	9.735×10^{-2}	0.0205	1.30	1.0000	0.34
	25	8.992×10^{-3}	0.449	0.9989	3.34	2.816×10^{-3}	1.27	0.9999	0.91	5.925×10^{-2}	0.0231	1.25	0.9999	0.90
	50	6.970×10^{-3}	0.330	0.9993	2.85	1.742×10^{-3}	1.21	0.9999	0.98	3.684×10^{-2}	0.0265	1.20	0.9997	1.71
N_2	0	2.257×10^{-3}	0.350	1.0000	0.42	5.973×10^{-4}	1.16	0.9990	2.83	3.074×10^{-2}	0.0098	1.18	0.9992	3.29
	25	8.833×10^{-4}	0.600	0.9996	1.37	3.447×10^{-4}	1.25	0.9965	4.43	8.893×10^{-3}	0.0179	1.25	0.9973	4.65
	50	4.402×10^{-4}	0.820	0.9989	1.56	2.026×10^{-4}	1.43	0.9921	7.35	4.294×10^{-3}	0.0184	1.33	0.9924	5.95
AAC2														
CO_2	0	1.107×10^{-2}	1.023	0.9953	5.81	5.722×10^{-3}	1.53	1.0000	0.38	9.640×10^{-2}	0.0169	1.47	1.0000	0.13
	25	7.376×10^{-3}	0.860	0.9967	4.42	3.492×10^{-3}	1.45	1.0000	0.50	1.031×10^{-1}	0.0084	1.42	1.0000	0.24
	50	6.602×10^{-3}	0.490	0.9960	5.46	2.168×10^{-3}	1.36	0.9999	0.64	4.946×10^{-2}	0.0170	1.32	1.0000	0.31
N_2	0	2.867×10^{-3}	0.300	0.9995	1.46	6.673×10^{-4}	1.18	0.9988	2.94	9.003×10^{-2}	0.0031	1.18	0.9989	2.94
	25	1.442×10^{-3}	0.400	0.9999	0.37	4.154×10^{-4}	1.25	0.9981	4.85	4.296×10^{-2}	0.0038	1.20	0.9984	3.70
	50	8.500×10^{-4}	0.400	0.9979	2.53	2.448×10^{-4}	1.25	0.9965	4.43	1.240×10^{-2}	0.0071	1.27	0.9970	4.92

In addition, n_f and n_s values obtained for activated carbons vary between 1 and 2 (1.64–1.77, 1.41–1.61, 1.21–1.35 and 1.36–1.53 for n_f and 1.61–1.73, 1.36–1.53, 1.20–1.30 and 1.32–1.47 for n_s corresponding to OAC1, OAC2, AAC1 and AAC2, respectively), demonstrating that the CO_2 adsorption is a physisorption and favourable. Also, the values of $1/n_f$ and $1/n_s$ were all found to be lower than 1 at various temperatures, offering a satisfactory adsorption intensity [65]. For N_2 adsorption, the values of n_f and n_s are similar, independently of the carbon used, showing low influence of surface characteristics upon the adsorption of this gas. Considering the Freundlich model, the values of k_f for all carbons and both gases decreased with increasing temperature showing again a physisorption behavior. The reduction of CO_2 and N_2 adsorption capacities is contributed to favourability of endothermic desorption process at high temperatures. In general, the maximum CO_2 and N_2 adsorption capacities (q_m) determined by the Langmuir equation decreased with increasing temperature, which confirms the exothermic nature of the adsorption process as reported in literature [65–68]. With respect to the parameter b for CO_2 adsorption, in general, higher values were found at 0 °C indicating that at this temperature the gas molecules are more attracted to the carbon's surface, in accordance to the higher adsorption capacities at this temperature [69].

3.3. CO_2/N_2 selectivity

Several studies [50,70] have estimated the selectivity reached in a gas separation operation using pure compounds adsorption data as shown in Fig. 6. Selectivity is considered a very important parameter in separation operations that allows to reach at least one stream with a high purity. A typical composition of a post-combustion stream generally shows a low CO_2 concentration, and it can be considered 14 % CO_2 and 86 % N_2 [38]. Then, the partial pressure of each gas can be calculated, and the amount of each gas adsorbed in the solid can be estimated. These values were used to calculate the apparent selectivity of each material to remove CO_2 by using Eq. (11) and the results obtained are listed in Table 11.

$$S_{CO_2/N_2} = \frac{n_{CO_2}/P_{CO_2}}{n_{N_2}/P_{N_2}} \quad (11)$$

where n and P refer to the number of moles and partial pressure of carbon dioxide and nitrogen in the CO_2/N_2 stream, respectively.

These selectivity values are suitable for gas separation but this procedure for selectivity determination using pure component adsorption data must be considered as a conservative estimation [38] because the presence of both gases in contact with the solid tends to increase selectivity due to the competitive behavior for adsorption sites. Thus, the adsorbed CO_2/N_2 ratio is expected to increase due to the higher affinity of CO_2 for the adsorbent surface.

Moreover, based on apparent selectivity data, the porous structure characteristics are also important for the separation of these gases. A clear increase in selectivity is observed for almond shell-based carbons with the higher percentage of microporosity. For olive stone-based carbons, a different behavior is observed mainly for the activated carbon with a carbon/KOH ratio of 1:4 w/w with an enhancement in CO_2 separation in comparison with the almond shell carbon prepared with the same procedure. This enhancement is in agreement with the higher CO_2 adsorption found at low pressure (as the CO_2 partial pressure in post-combustion stream) for this material (Fig. 6).

The analysis of the selectivity of the carbons prepared to be used in CO_2/N_2 separation operations by gas–solid adsorption has been completed by using the ideal adsorption solution theory (IAST) that is commonly used for this type of evaluation and considered useful for pressure swing adsorption operation design [71,72]. The use of this theory involves several assumptions [73,74] but it allows to estimate separation selectivity considering the influence of the presence of other gases upon the adsorption capacity of each component. This type of calculation has been carried out using the software package GraphIAST [75].

Fig. 8 shows the estimated values of gas selectivity using IAST. These data allow to confirm that olive stone activated carbon with a carbon/KOH ratio of 1:4 w/w (OAC1) shows the highest value for CO_2 selectivity and is influenced by binary feed stream on account of its high CO_2 adsorption capacity. The most important difference of this carbon in relation with the others is the large amount of oxygen (see Tables 3 and 4) after activation that could generate an important presence of oxygen-containing functional groups such as carboxylic and hydroxyl groups that enhances CO_2 adsorption [76]. Non-activated carbons also indicate high CO_2 selectivity which is in agreement to the values obtained for apparent selectivity (Table 11) corresponding to these materials. The activated carbons for both raw materials with a carbon/KOH ratio of 1:2 w/w (AAC2 and OAC2) show a similar behaviour with relatively low selectivity values. On the other hand, the activated carbon fabricated from almond shells with a carbon/KOH ratio of 1:4 w/w (AAC1) shows the lowest value for IAST selectivity like that included in Table 11. These data confirm that the type of precursor employed to fabricate the carbon can generate important differences that are explained based on the different shape of CO_2 adsorption isotherms previously analyzed (see Fig. 6).

Taking into account the conclusions achieved in previous studies [52,53] about the great importance of low-size pores in the adsorption of specific gases such as carbon dioxide, an analysis of PSD influence upon CO_2 selectivity has been carried out. The overall analysis of these data allows to point out the important role of low-size ultramicropores ($D_p <$ 4.5 Å) upon CO_2 selectivity in adsorption of CO_2/N_2 gaseous streams. This type of influence can be observed in Fig. S4 showing an increase in CO_2 selectivity with the amount of volume generated by low-size ultramicropores.

Table 11
Selectivity values for CO_2/N_2 at 25 °C for a typical post-combustion stream (14 % CO_2 and 86 % N_2).

Waste	Material	Apparent selectivity
Olive stones	OC	33.1
	OAC2	14.6
	OAC1	21.1
Almond Shells	AC	33.2
	AAC2	14.5
	AAC1	11.7

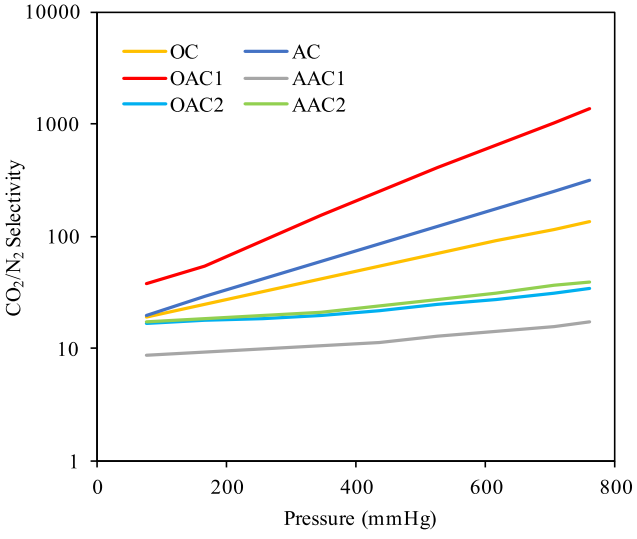

Fig. 8. IAST selectivity estimation for a post-combustion stream (14% CO_2 and 86% N_2) using the materials developed in the present work.

3.4. Effect of temperature - heat of adsorption

As seen from Fig. 6, the influence of temperature on CO_2 and N_2 adsorption is similar for all the carbons fabricated, showing a decrease in the amount of gas adsorbed with increasing temperature, which is in agreement with the presence of weak interactions between gases and carbon surface [77] that would allow to reach a suitable carbon regeneration, that is an important part of the overall separation operation. In all cases, the amount of CO_2 adsorbed at each pressure is much higher than for N_2 that allows to use these materials for the separation of these gases at different temperatures and avoiding the necessity of a strict temperature conditioning step. Anyway, a lower temperature allows to enhance carbon dioxide adsorption, which confirms that this variable must be analyzed to perform a suitable gas separation by adsorption.

The experimental data for CO_2 and N_2 adsorption isotherms at different temperatures have been used to determine the isosteric heat of adsorption involved on the mass transfer process, which is one of the most crucial factors in designing and developing a gas separation process by adsorption. Heat of adsorption has been computed for the carbons with the better CO_2 selectivity values and this parameter was calculated at different amounts of adsorbed gas (see Fig. 9) based on the Clausius-Clapeyron equation (Eq. (12)).

$$lnP = \left(\frac{-Q_{st}}{R}\right)\frac{1}{T} + C \tag{12}$$

where Q_{st} is the isosteric heat of adsorption (kJ mol^{-1}) which is calculated from the slope of the plot of lnP versus $1/T$, R is the universal gas constant (8.314 J mol^{-1} K^{-1}), T is the temperature (K), P refers to the pressure of the gas, and C is a constant which can be determined from the intercept value.

In general, Fig. 9 shows that CO_2 adsorption involves higher heat of adsorption values than N_2 adsorption. This behavior agrees with previous studies [78] that conclude a higher affinity of carbons for CO_2 involving stronger interactions. Though larger values of heat of adsorption were obtained for carbon dioxide adsorption compared to nitrogen, in general, these values are low for all carbons and both gases that are compatible with a physical adsorption process, which is also in agreement with previous conclusions reached in the adsorption isotherms, and a suitable behavior for its use for gas separation.

Analyzing the heat of adsorption associated with CO_2, it is observed that the non-activated carbons showed higher values (between 25 and 30 kJ mol^{-1}) than the activated ones (between 20 and 25 kJ mol^{-1}). This behavior can be explained by the reduction in functional groups in carbon surface during the activation process which leads to a decrease in the interaction's intensity between adsorbate and adsorbent.

In addition, a higher amount of adsorbed CO_2 tends to produce a slight decrease in the value of heat of adsorption. This behavior is related to the higher affinity of CO_2 for the small size pores where interactions are enhanced [79].

In relation to the heat of adsorption of N_2, a slight influence of the type of carbon and gas adsorption was observed due to the presence of low intensity interactions between the gas and carbon surface. The effect of gas adsorption upon heat of adsorption for N_2 shows the opposite behaviour to that previously indicated for CO_2, since heat of adsorption slightly increases with increasing the adsorbed amount, which can be explained by the preferential interactions with the molecules previously adsorbed on the carbon surface [80].

3.5. CO_2 mass transfer coefficient

The mass transfer coefficient together with the adsorption isotherms are the main factors for the simulation of CO_2 capture. After fitting the experimental data corresponding to the CO_2 adsorption kinetics using the linear and quadratic driving force models and performing the non-linear regression analysis as shown in Figs. S5 (A-D) and S6 (A-D), the quadratic model for all the carbons was found to be more slightly appropriate according to the higher R^2 and lower MRAD values shown in Table S2 and, therefore, this model was used for the simulation of binary dynamic breakthrough experiments. The CO_2 mass transfer coefficients determined using the quadratic model for the carbons selected based on selectivity was obtained as 0.0040, 0.0062, 0.0034, and 0.0062 s^{-1} at

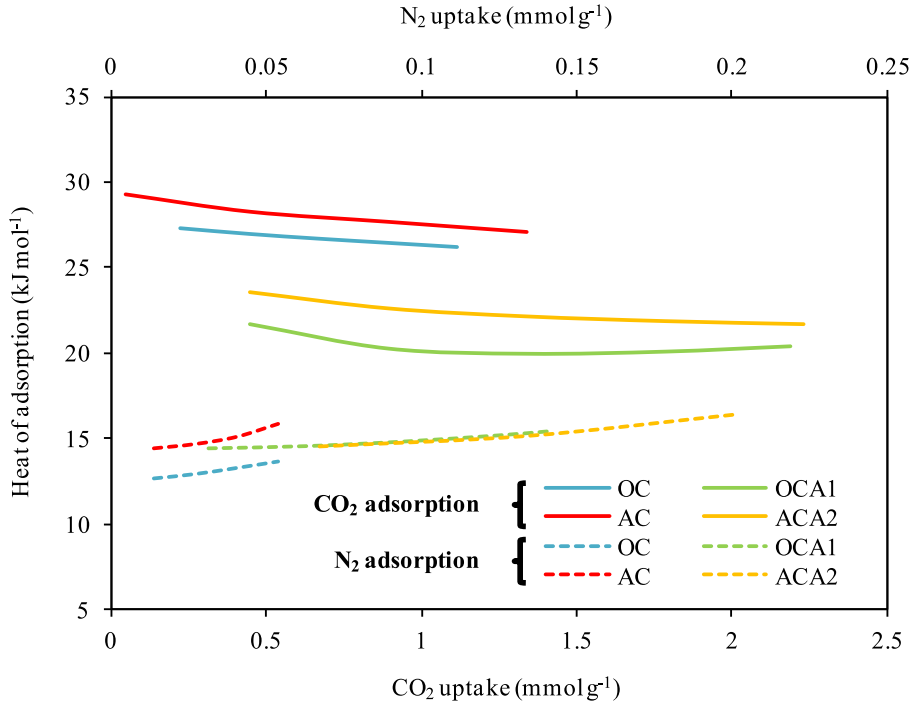

Fig. 9. Effect of gas adsorption values upon isosteric heat of adsorption.

25 °C and 0.0080, 0.0100, 0.0046, and 0.0092 s^{-1} at 50 °C for AC, OC, AAC2, and OAC1, respectively, as shown in Tables 12 and S2 together with the amount adsorbed of CO_2 at equilibrium (0.0016, 0.0015, 0.0028, and 0.0022 kmol kg^{-1} at 25 °C and 0.0010, 0.0010, 0.0017, and 0.0014 kmol kg^{-1} at 50 °C for AC, OC, AAC2, and OAC1, respectively) as fitting parameters (Table S2). A higher mass transfer coefficient indicates faster adsorption rate between the CO_2 and carbon to reach equilibrium. These values are significantly low in comparison with the mass transfer coefficients determined using linear driving force model for physically activated carbons fabricated from olive stones and almond shells [38], which could be desirable for the fast-swing processes. In addition, the values obtained in the present work are agreement with the average value calculated by Jribi et al. [81] using activated carbon.

The best fitting results obtained for the quadratic model agree with previous studies [82] that confirmed the suitability of this model for materials with large microporosity for which the diffusion inside the sorbent is considered the controlling stage. The behaviour observed for the linear driving force model (Fig. S5) suggest that this model overestimates the adsorption data at short times and underestimates them at large times [83].

In general, the mass transfer coefficients for activated carbons from both precursors do not increase with activation because microporosity increases (see Table 8) and gas diffusion in the porous structure decreases in the presence of micropores. Olive stone-based carbons (with and without activation) reached higher values for mass transfer coefficient due to their lower microporosity.

3.6. Binary dynamic breakthrough simulations

Dynamic breakthrough simulations for the separation of a mixture of 14 % CO_2 and 86 % N_2 were performed in a fixed-bed column using the carbons with the higher CO_2/N_2 selectivity (see section 3.3) over a range of temperatures and feed flow rates to evaluate the performance of the carbons on the adsorption capacity of CO_2 and achieve a high level of purity and recovery for both gases. The breakthrough time was considered at which the CO_2 concentration in the outlet stream is 0.1 % molar and nitrogen is recovered with a high purity of 99.9 %. The main characteristics of the adsorption column, adsorbents and operational conditions used for the simulation of binary dynamic adsorption experiments are given in Table 12.

Bed and particle porosities ($\varnothing_b$ and $\varnothing_P$) and densities (ρ_b and ρ_P) were calculated using Eqs. (13–16), respectively.

$$\varnothing_b = \frac{V_T - (V_P + V_S)}{V_T} \tag{13}$$

Table 12
Characteristics of adsorption column, adsorbents and operational conditions for binary breakthrough simulations.

Characteristic	OC	AC	OAC1	AAC2
Bed porosity (%)	57.7	57.5	67.9	49.7
Particle porosity (%)	23.1	22.5	76.9	77.4
Bed density (kg m^{-3})	532	555	195	345
Solid density (kg m^{-3})	1636	1686	2643	3045
Particle density (kg m^{-3})	1258	1307	609	687
Mass of the adsorbent (g)	18.8	19.6	6.9	12.2
CO_2 mass transfer coefficient at 25 °C (s^{-1})	0.0062	0.0040	0.0062	0.0034
CO_2 mass transfer coefficient at 50 °C (s^{-1})	0.0100	0.0080	0.0092	0.0046
Isotherm model (-)	Langmuir	Langmuir	Freundlich	Sips
Operational conditions				
Adsorption pressure (bar)	1.013			
Adsorption temperature (°C)	25 and 50			
Feed flow rate (sccm)	60, 120, 180 and 240			
Feed stream composition (molar fraction)	0.14 for CO_2 and 0.86 for N_2			

$$\varnothing_P = \frac{V_P}{(V_P + V_S)} \tag{14}$$

$$\rho_b = \frac{m_P}{V_T} \tag{15}$$

$$\rho_P = \frac{m_P}{(V_P + V_S)} \tag{16}$$

where V_T is the total volume of the column (m^3), m_P is the mass of carbon particles packed in the column (kg), and V_P and V_S refer to the pore and solid volumes of the particles (m^3), respectively.

In real experiments, a primary stage of degasification is done on the adsorbents packed in the column before running dynamic breakthrough experiments to remove any oxygen and humidity. Therefore, it was assumed that the adsorption column is full of helium at initial conditions.

Fig. 10 shows the influence of the feed flow rate on the CO_2/N_2 breakthrough curve of the adsorbents at 25 °C and 1.013 bar. As can be seen, nitrogen reaches the outlet of the column immediately owing to its very slow diffusion rate into the pores whereas the breakthrough time for CO_2 is much higher which is related to its greater adsorption capacity and selectivity on the carbons fabricated compared to N_2. This difference in the adsorption capacity and selectivity of gases in a binary dynamic system agrees with the experimental data obtained from the pure component adsorption isotherms previously discussed. A reduction in the feed flow rate from 240 to 60 sccm led to increase the CO_2 breakthrough time from 95 to 1045 s for OC, 2990 to 13360 s for OAC1, 50 to 800 s for AC and 1790 to 9890 s for AAC2. This is because it takes much longer time to saturate the adsorption column using a low feed flow rate which can improve mass transfer between CO_2 and the adsorbents. In addition, based on the shape of breakthrough curves, it is possible to observe that low flow rates show a clear increase in the length of the adsorption zone.

After reaching the breakthrough time, an additional time is needed to reach the bed saturation. But, it is preferred to end the experiments at the breakthrough time to obtain a high purity for N_2 in the outlet, although a little more CO_2 could be adsorbed on the adsorbents between the breakthrough and saturation times. At the breakthrough time, the CO_2 adsorption efficiency was obtained as 99.8 % and 99.2 % for activated carbons and non-activated ones, respectively. The activated carbon fabricated from olive stones using a carbon/KOH of 1:4 w/w (OAC1) was found to have a greater N_2 recovery factor (96.8 %) followed by AAC2 (92.7 %), OC (87.4 %) and AC (85.9 %). Moreover, binary dynamic simulations demonstrated that OAC1 can adsorb CO_2 with the highest purity (84.3 %) compared to 69.8 %, 59.1 %, 56.0 % for AAC2, OC and AC, respectively. This can confirm the high selectivity of OAC1 in a multicomponent system which is in agreement with the selectivity data obtained using IAST as discussed above. In the case of OC and AC, despite the high selectivity of CO_2 obtained using the pure component equilibrium adsorption data, these non-activated carbons are affected by binary feed stream due to their low CO_2 adsorption capacity (0.33 mmol g^{-1} for OC and 0.32 mmol g^{-1} for AC) which resulted in a reduction in the CO_2 purity in comparison with the activated ones. The CO_2 and N_2 adsorption capacities for OAC1 were determined to be 1.05 and 0.15 mmol g^{-1}, respectively, which indicates a high selectivity and purity of CO_2. On the other hand, the adsorption capacities of CO_2 and N_2 for AAC2 were 0.86 and 0.25 mmol g^{-1}. The higher selectivity of OAC1 compared to AAC2 is related to its greater pore volume and surface area (see Table 8).

Breakthrough curves for CO_2 and N_2 were also obtained at 50 °C, which could be a feasible temperature for a flue gas stream in desulfurization units, to evaluate the effect of temperature on the CO_2 adsorption capacity and selectivity as can be seen in Fig. 11. An increase in temperature led to a decrease in the breakthrough time of CO_2. This is because adsorption is an exothermic process and then, the CO_2

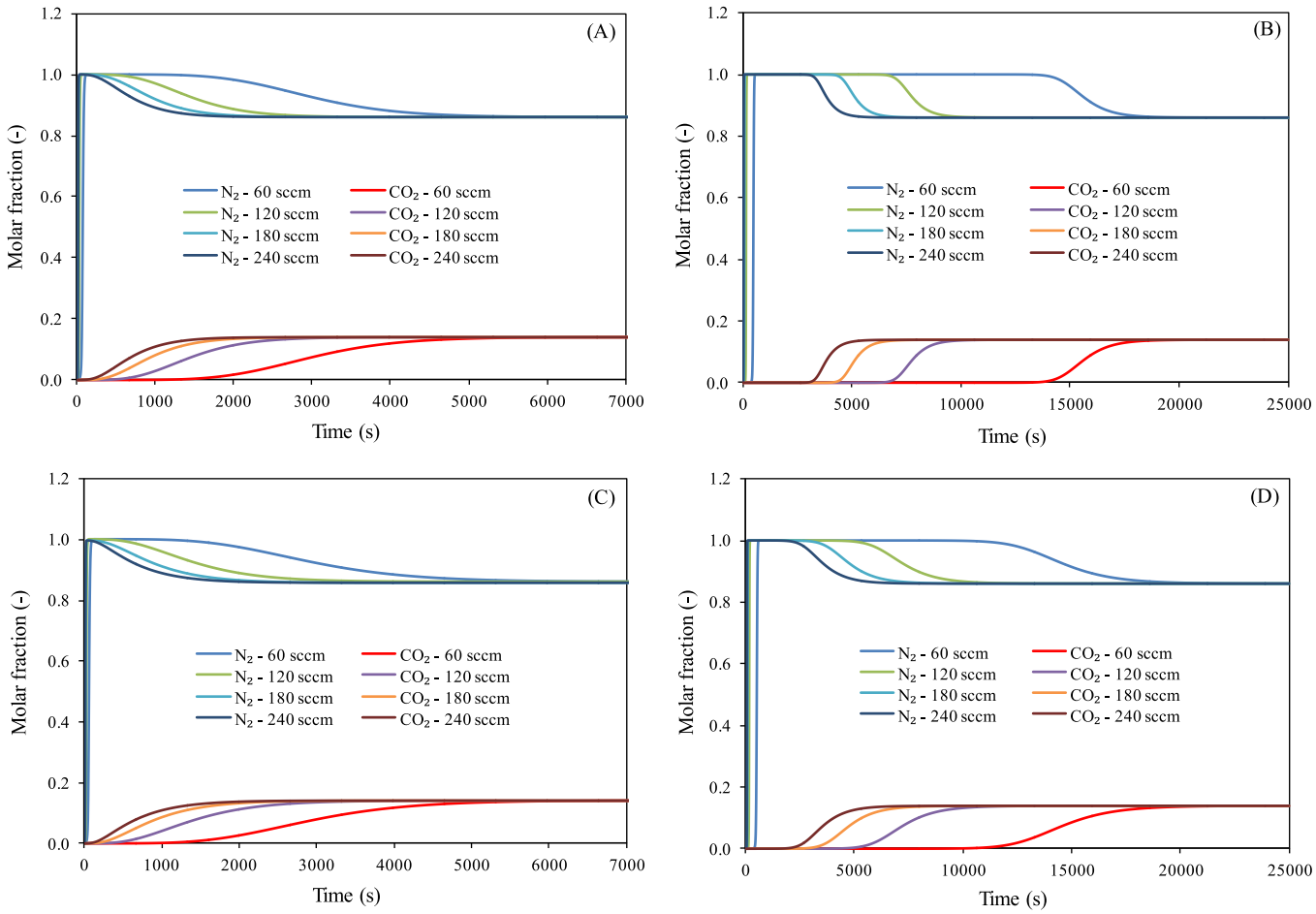

Fig. 10. CO_2/N_2 breakthrough curve of the carbons at various feed flow rates: (A)- OC, (B)- OAC1, (C)- AC and (D)- AAC2. (T = 25 °C).

adsorption capacity is reduced when temperature is increased. As expected, OAC1 was found to have the highest breakthrough time (8640 s) and CO_2 adsorption capacity (0.67 mmol g^{-1}). This carbon showed better results than those found for a physically activated carbon based on olive stones [38]. For the other materials analyzed, breakthrough time and CO_2 adsorption capacity were 4540 s and 0.48 mmol g^{-1} for AAC2, 50 s and 0.10 mmol g^{-1} for OC and 40 s and 0.08 mmol g^{-1} for AC. The results obtained also revealed that for activated carbons the CO_2 purity at the breakthrough time (81.3 % for OAC1 and 64.6 % for AAC2) is not significantly influenced by the rise in the temperature from 25 to 50 °C whereas its impact for non-activated ones was considerably high (40.5 % for OC and 35.0 % for AC). The nitrogen recovery factor of OAC1 was obtained as 96.7 % which was the greatest compared to the other carbons at 50 °C (90.6, 70.7 and 62.9 % for AAC2, OC and AC, respectively).

In summary, the chemically activated carbon fabricated from olive stones as a cheap biomass waste using potassium hydroxide with a carbon/KOH ratio of 1:4 (w/w) was found to be an efficient adsorbent to separate CO_2 from N_2 under post-combustion conditions possessing the higher CO_2 adsorption capacity, CO_2/N_2 selectivity, CO_2 purity and N_2 recovery factor in comparison to the other carbons fabricated in the present work.

4. Conclusions

The carbons fabricated from olive stones and almond shells as biomass precursors with a low cost and high availability are able to capture CO_2 from N_2 at atmospheric pressure from post-combustion streams. Although the activation process using KOH resulted in modifications in the surface and small-size pores of the activated carbons, they could maintain a significant amount of pores in the microporosity range. The equilibrium adsorption isotherms of pure CO_2 and N_2 revealed that the CO_2 adsorption capacity is significantly higher than that of N_2. Furthermore, an increase in temperature from 0 to 50 °C led to a reduction in the adsorption capacity of CO_2 for the carbons due to the exothermic character of the adsorption process.

The non-activated carbons were found to have a higher CO_2/N_2 apparent selectivity obtained from pure components equilibrium data than to the activated ones. The highest selectivity was obtained for AC followed by OC, OAC1 and AAC2. However, the results obtained from IAST selectivity calculations and dynamic breakthrough simulations at 25 °C demonstrated that non-activated carbons selectivity is remarkably influenced by a binary stream fed to the column on account of their significantly lower CO_2 adsorption capacity in comparison with the activated ones. Moreover, the highest CO_2/N_2 selectivity in the binary system was obtained for OAC1 which was in agreement with the selectivity data obtained from IAST that could be enhanced by the high presence of low-size ultramicropores and oxygen-containing surface functional groups. Reducing the feed flow rate from 240 to 60 sccm resulted in an increase in the amount of CO_2 breakthrough time for the adsorbents due to the longer time required for saturation of the adsorption column applying a lower feed flow rate which can enhance the mass transfer between CO_2 and the carbons. OAC1 was found to have a higher CO_2 breakthrough time compared to the other carbons. An increase in the adsorption temperature from 25 to 50 °C led to a reduction in the CO_2 breakthrough time and adsorption capacity in the dynamic multicomponent system which was in agreement with the equilibrium data obtained for pure components. OAC1 could be

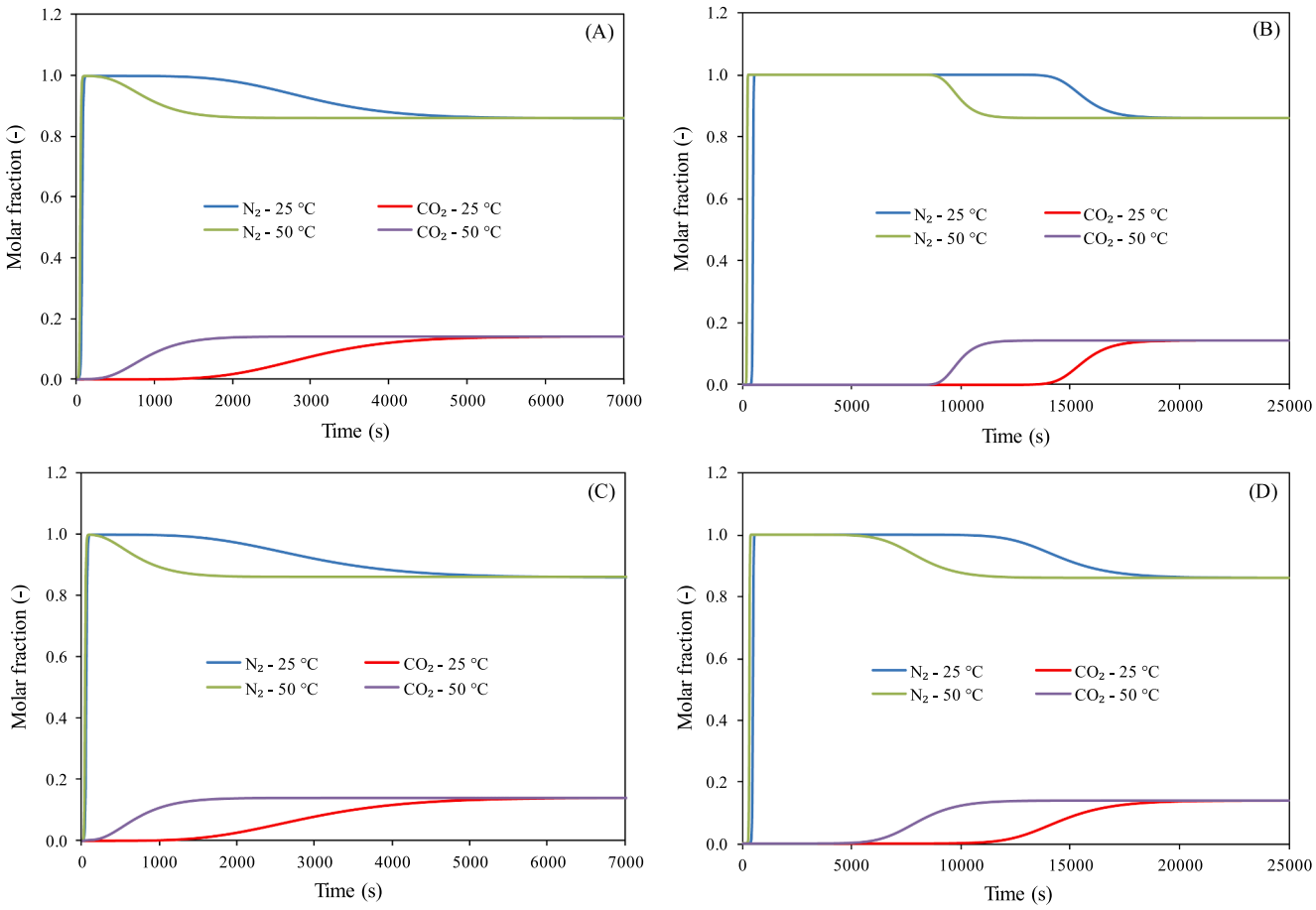

Fig. 11. Effect of temperature on the CO_2/N_2 breakthrough curve of the carbons: (A)- OC, (B)- OAC1, (C)- AC and (D)- AAC2. (Feed flow rate = 60 sccm).

considered as the most promising adsorbent with the highest CO_2 adsorption capacity and selectivity to separate CO_2 (14 %) and N_2 (86 %) from a flue gas stream at 25 and 50 °C (a typical temperature for desulfurization units) under post-combustion conditions. In addition to these positive characteristics, this carbon shows the lowest heat of adsorption that can improve the desorption stage necessary to implement the adsorption process at industrial scale.

CRediT authorship contribution statement

Vahid Rahimi: Writing – review & editing, Writing – original draft, Software, Methodology, Investigation, Conceptualization, Formal analysis, Visualization. **Adrián Ferreiro-Salgado:** Investigation, Formal analysis. **Diego Gómez-Díaz:** Writing – review & editing, Writing – original draft, Supervision, Methodology, Investigation, Conceptualization. **María Sonia Freire:** Conceptualization, Investigation, Supervision, Writing – review & editing. **Julia González-Álvarez:** Writing – review & editing, Supervision, Project administration, Funding acquisition.

Declaration of competing interest

The authors declare that they have no known competing financial interests or personal relationships that could have appeared to influence the work reported in this paper.

Data availability

The research data supporting this publication are provided within this paper

Acknowledgements

This work is part of I + D + i project Reference PID2021-122923NB-I00 financed by MCIN/AEI /10.13039/501100011033 / FEDER, UE. Authors would like to thank the use of RIAIDT-USC analytical facilities. Authors would also like to thank Dr. Carlos A. Pena and Dr. A. Gil for their helps in performing the kinetic experiments and determining the solid density of carbons, respectively.

Appendix A. Supplementary data

Supplementary data to this article can be found online at https://doi.org/10.1016/j.seppur.2024.127110.

References

[1] M. Songolzadeh, M. Soleimani, M. Takht Ravanchi, R. Songolzadeh, Carbon dioxide separation from flue gases: a technological review emphasizing reduction in greenhouse gas emissions, The Sci. World J. (2014) 828131, https://doi.org/10.1155/2014/828131.
[2] R.K. Pachauri, L.A. Meyer, IPCC. Climate Change 2014: Synthesis Report. Contribution of Working Groups I, II and III to the Fifth Assessment Report of the Intergovernmental Panel on Climate Change, Core Writing Team. (Eds.), IPCC, Geneva, Switzerland, 2014.
[3] S. Wang, G. Li, C. Fang, Urbanization, economic growth, energy consumption, and CO_2 emissions: Empirical evidence from countries with different income levels, Renew. Sustain. Energy Rev. 81 (2018) 2144–2159, https://doi.org/10.1016/J.RSER.2017.06.025.
[4] F. Sher, M.A. Pans, C. Sun, C. Snape, H. Liu, Oxy-fuel combustion study of biomass fuels in a 20 kWth fluidized bed combustor, Fuel 215 (2018) 778–786, https://doi.org/10.1016/j.fuel.2017.11.039.
[5] F. Sher, M.A. Pans, D.T. Afilaka, C. Sun, H. Liu, Experimental investigation of woody and non-woody biomass combustion in a bubbling fluidised bed combustor focusing on gaseous emissions and temperature profiles, Energy 141 (2017) 2069–2080, https://doi.org/10.1016/j.energy.2017.11.118.

[6] I.U. Hai, F. Sher, G. Zarren, H. Liu, Experimental investigation of tar arresting techniques and their evaluation for product syngas cleaning from bubbling fluidized bed gasifier, J. Clean. Prod. 240 (2019) 118239, https://doi.org/10.1016/j.jclepro.2019.118239.

[7] E.I. Koytsoumpa, C. Bergins, E. Kakaras, The CO_2 economy: review of CO_2 capture and reuse technologies, J. Supercrit. Fluids 132 (2018) 3–16, https://doi.org/10.1016/J.SUPFLU.2017.07.029.

[8] M.D. Aminu, S.A. Nabavi, C.A. Rochelle, V. Manovic, A review of developments in carbon dioxide storage, Appl. Energy 208 (2017) 1389–1419, https://doi.org/10.1016/J.APENERGY.2017.09.015.

[9] L. Nord, O. Bolland, Carbon dioxide emission management in power generation, Wiley-VCH Verlag GmbH & Co., Weinheim, Germany, 2020.

[10] E.S. Sanz-Pérez, C.R. Murdock, S.A. Didas, C.W. Jones, Direct capture of CO2 from ambient air, Chem. Rev. 116 (2016) 11840–11876, https://doi.org/10.1021/acs.chemrev.6b00173.

[11] P. Madejski, K. Chmiel, N. Subramanian, T. Kus, Methods and techniques for CO_2 capture: Review of potential solutions and applications in modern energy technologies, Energies 15 (2022) 887, https://doi.org/10.3390/en15030887.

[12] M. Bui, C.S. Adjiman, A. Bardow, E.J. Anthony, A. Boston, S. Brown, et al., Carbon capture and storage (CCS): the way forward, Energy Environ. Sci. 11 (2018) 1062–1076, https://doi.org/10.1039/C7EE02342A.

[13] S. Fakher, A. Imqam, Application of carbon dioxide injection in shale oil reservoirs for increasing oil recovery and carbon dioxide storage, Fuel 265 (2020) 199–207, https://doi.org/10.1016/j.fuel.2019.116944.

[14] S. Tian, F. Yan, Z. Zhang, J. Jiang, Calcium-looping reforming of methane realizes in situ CO_2 utilization with improved energy efficiency, Sci. Adv. 5 (2019) eaav5077, https://doi.org/10.1126/sciadv.aav5077.

[15] J.C. Abanades, E.S. Rubin, M. Mazzotti, H.J. Herzog, On the climate change mitigation potential of CO_2 conversion to fuels, Energy Environ. Sci. 10 (2017) 2491–12249, https://doi.org/10.1039/C7EE02819A.

[16] Energy Technology Perspectives 2020, Special report on carbon capture utilisation and storage CCUS in clean energy transitions, IEA, Paris, France, 2020.

[17] Y. Wang, L. Zhao, A. Otto, M. Robinius, D. Stolten, A review of post-combustion CO_2 capture technologies from coal-fired power plants, Energy Procedia 114 (2017) 650–665, https://doi.org/10.1016/j.egypro.2017.03.1209.

[18] J.D. Figueroa, T. Fout, S. Plasynski, H. McIlvried, R.D. Srivastava, Advances in CO_2 capture technology—The U.S. department of energy's carbon sequestration program, Int. J. Greenh. Gas Control 2 (2008) 9–20, https://doi.org/10.1016/S1750-5836(07)00094-1.

[19] B. Metz, O. Davidson, H.C. de Coninck, M. Loos, L.A. Meyer, IPCC. Special report on carbon dioxide capture and storage. Prepared by Working Group III of the Intergovernmental Panel on Climate Change (Eds.), Cambridge University Press: Cambridge, UK, and New York, 2005.

[20] E. Tzimas, S. Peteves, Controlling carbon emissions, The option of carbon sequestration, EUR 20752 EN, European Commission, 2003 JRC25489. https://publications.jrc.ec.europa.eu/repository/handle/JRC25489.

[21] R. Gaikwad, W.L. Boward, W. DePriest, Wet flue gas desulfurization technology evaluation. Sargent & Lundy, LLC: Chicago, IL, 2003.

[22] L.A. Darunte, K.S. Walton, D.S. Sholl, C.W. Jones, CO_2 capture via adsorption in amine-functionalized sorbents, Curr. Opin. Chem. Eng. 12 (2016) 82–90, https://doi.org/10.1016/j.coche.2016.03.002.

[23] G.T. Rochelle, Conventional amine scrubbing for CO_2 capture, In absorption-based post-combustion capture of carbon dioxide, Feron PHM (Eds.), Woodhead Publishing, Cambridge, UK, 2016, Chap 3, pp. 35–67.

[24] P. Tontiwachwuthikul, R. Idem, Recent progress and new developments in post combustion carbon-capture technology with reactive solvents, In recent progress and new developments in post-combustion carbon capture technology with reactive solvents. Tontiwachwuthikul P, Idem R (Eds.), Future Science Book Series, 2013, pp. 2–8.

[25] X. Wang, C. Song, Carbon capture from flue gas and the atmosphere: a perspective, Front. Energy Res. 8 (2020) 560849, https://doi.org/10.3389/fenrg.2020.560849.

[26] B. Li, Y. Duan, D. Luebke, B. Morreale, Advances in CO2 capture technology: a patent review, Appl. Energy 102 (2013) 1439–1447, https://doi.org/10.1016/j.apenergy.2012.09.009.

[27] A. Samanta, A. Zhao, G.K.H. Shimizu, P. Sarkar, R. Gupta, Post-combustion CO2 capture using solid sorbents: a review, Ind. Eng. Chem. Res. 51 (2012) 1438–1463, https://doi.org/10.1021/ie200686q.

[28] A. Sayari, Y. Belmabkhout, R. Serna-Guerrero, Flue gas treatment via CO2 adsorption, Chem. Eng. J. 171 (2011) 760–774, https://doi.org/10.1016/j.cej.2011.02.007.

[29] F. Montagnaro, A. Silvestre-Albero, J. Silvestre-Albero, F. Rodríguez-Reinoso, A. Erto, A. Lancia, et al., Post-combustion CO2 adsorption on activated carbons with different textural properties, Micropor. Mesopor. Mat. 209 (2015) 157–164, https://doi.org/10.1016/j.micromeso.2014.09.037.

[30] Z. Chen, S. Deng, H. Wei, B. Wang, J. Huang, G. Yu, Activated carbons and amine-modified materials for carbon dioxide capture — a review, Front, Environ. Sci. Eng. 7 (2013) 326–340, https://doi.org/10.1007/s11783-013-0510-7.

[31] L. Estevez, D. Barpaga, J. Zheng, S. Sabale, R.L. Patel, J.-G. Zhang, et al., Hierarchically porous carbon materials for CO2 capture: The role of pore structure, Ind. Eng. Chem. Res. 57 (2018) 1262–11128, https://doi.org/10.1021/acs.iecr.7b03879.

[32] D. Xu, P. Xiao, J. Zhang, G. Li, G. Xiao, P.A. Webley, et al., Effects of water vapour on CO2 capture with vacuum swing adsorption using activated carbon, Chem. Eng. J. 230 (2013) 64–72, https://doi.org/10.1016/j.cej.2013.06.080.

[33] G. Gautam, S. Kumar, Sahoo, Performance improvement and comparisons of CO_2 based adsorption cooling system using modified cycles employing various adsorbents: a comprehensive study of subcritical and transcritical cycles, Int. J. Refrig. 112 (2020) 136–154, https://doi.org/10.1016/j.ijrefrig.2019.12.008.

[34] H.A. Patel, F. Karadas, J. Byun, J. Park, E. Deniz, A. Canlier, et al., Highly stable nanoporous sulfur-bridged covalent organic polymers for carbon dioxide removal, Adv. Funct. Mater. 23 (2013) 2270–3226, https://doi.org/10.1002/adfm.201202442.

[35] M.G. Plaza, C. Pevida, B. Arias, J. Fermoso, M.D. Casal, C.F. Martín, et al., Development of low-cost biomass-based adsorbents for postcombustion CO2 capture, Fuel 88 (2009) 2442–12247, https://doi.org/10.1016/j.fuel.2009.02.025.

[36] M.G. Plaza, C.F. Pevida, C.F. Martín, J. Fermoso, J.J. Pis, F. Rubiera, Developing almond shell-derived activated carbons as CO2 adsorbents, Sep. Purif. Technol. 71 (2010) 102–116, https://doi.org/10.1016/j.seppur.2009.11.008.

[37] M.G. Plaza, S. García, F. Rubiera, J.J. Pis, C. Pevida, Evaluation of ammonia modified and conventionally activated biomass based carbons as CO2 adsorbents in postcombustion conditions, Sep. Purif. Technol. 80 (2011) 96–104, https://doi.org/10.1016/j.seppur.2011.04.015.

[38] A.S. González, M.G. Plaza, F. Rubiera, C. Pevida, Sustainable biomass-based carbon adsorbents for post-combustion CO2 capture, Chem. Eng. J. 230 (2013) 456–465, https://doi.org/10.1016/j.cej.2013.06.118.

[39] C.H. Pimentel, L. Díaz-Fernández, D. Gómez-Díaz, M.S. Freire, J. González-Álvarez, Separation of CO_2 using biochar and KOH and $ZnCl_2$ activated carbons derived from pine sawdust, J. Environ. Chem. Eng. 11 (2023) 111378, https://doi.org/10.1016/j.jece.2023.111378.

[40] S.A.C. Carabineiro, T. Thavorn-amornsri, M.F.R. Pereira, P. Serp, J.L. Figueiredo, Comparison between activated carbon, carbon xerogel and carbon nanotubes for the adsorption of the antibiotic ciprofloxacin, Catal. Today 186 (2012) 29–34, https://doi.org/10.1016/j.cattod.2011.08.020.

[41] M. Danish, T. Ahmad, A review on utilization of wood biomass as a sustainable precursor for activated carbon production and application, Renew. Sustain. Energy Rev. 87 (2018) 1–21, https://doi.org/10.1016/j.rser.2018.02.003.

[42] A.A. Shiryaev, P. Pré, C. Pardanaud, V. Murzin, A. Averin, J.-N. Rouzaud, Microporosity and nanostructure of activated carbons: characterization by X-ray diffraction and scattering, Raman spectroscopy and transmission electron microscopy, Adsorption 29 (2023) 275–289, https://doi.org/10.1007/s10450-023-00406-x.

[43] M.A. Lillo-Ródenas, D. Cazorla-Amorós, A. Linares-Solano, Understanding chemical reactions between carbons and NaOH and KOH: An insight into the chemical activation mechanism, Carbon 41 (2003) 267–275, https://doi.org/10.1016/S0008-6223(02)00279-8.

[44] Q. Li, S. Liu, W. Peng, W. Zhu, L. Wang, F. Chen, et al., Preparation of biomass-derived porous carbons by a facile method and application to CO_2 adsorption, J. Taiwan Inst. Chem. Eng. 116 (2020) 128–136, https://doi.org/10.1016/j.jtice.2020.11.001.

[45] Y. Tadjenant, N. Dokhan, A. Barras, A. Addad, R. Jijie, S. Szunerits, et al., Graphene oxide chemically reduced and functionalized with KOH-PEI for efficient Cr(VI) adsorption and reduction in acidic medium, Chemosphere 258 (2020) 127316, https://doi.org/10.1016/j.chemosphere.2020.127316.

[46] Y.J. Zhang, Z.J. Xing, Z.K. Duan, M. Li, Y. Wang, Effects of steam activation on the pore structure and surface chemistry of activated carbon derived from bamboo waste, Appl. Surf. Sci. 315 (2014) 279–286, https://doi.org/10.1016/j.apsusc.2014.07.126.

[47] D. Peredo-Mancilla, C.M. Ghimbeu, B.-N. Ho, M. Jeguirim, C. Hort, D. Bessieres, Comparative study of the CH_4/CO_2 adsorption selectivity of activated carbons for biogas upgrading, J. Environ. Chem. Eng. 7 (2019) 103368, https://doi.org/10.1016/j.jece.2019.103368.

[48] H. Yi, F. Li, P. Ning, X. Tang, J. Peng, Y. Li, et al., Adsorption separation of CO_2, CH_4, and N_2 on microwave activated carbon, Chem. Eng. J. 215–216 (2013) 635–642, https://doi.org/10.1016/j.cej.2012.11.050.

[49] W. Liang, Z. Liu, J. Peng, X. Zhou, X. Wang, Z. Li, Enhanced CO_2 adsorption and $CO_2/N_2/CH_4$ selectivity of novel carbon composites CPDA@A-Cs, Energy Fuels 33 (2019) 493–502, https://doi.org/10.1021/acs.energyfuels.8b03637.

[50] R. Ojeda-López, E. Vilarrasa-García, D.C.S. Azevedo, C. Felipe, J.A. Cecilia, E. Rodríguez-Castellón, CO2 selectivity in CO2:CH4 and CO2:N2 mixtures on carbon microfibers (CMFs) and carbon microspheres (CMSs), Fuel 324 (2022) 124242, https://doi.org/10.1016/j.fuel.2022.124242.

[51] M. Thommes, K. Kaneko, A.V. Neimark, J.P. Olivier, F. Rodriguez-Reinoso, J. Rouquerol, et al., Physisorption of gases, with special reference to the evaluation of surface area and pore size distribution (IUPAC Technical Report), Pure Appl. Chem. 87 (2015) 1051–1069, https://doi.org/10.1515/pac-2014-1117.

[52] J.J. Manyà, B. González, M. Azuara, G. Arner, Ultra-microporous adsorbents prepared from vine shoots-derived biochar with high CO_2 uptake and CO_2/N_2 selectivity, Chem. Eng. J. 345 (2018) 631–669, https://doi.org/10.1016/j.cej.2018.01.092.

[53] J. Serafin, U. Narkiewicz, A.W. Morawski, R.J. Wróbel, B. Michalkiewicz, Highly microporous activated carbons from biomass for CO_2 capture and effective micropores at different conditions, J. CO_2 Util. 18 (2017) 73–79, https://doi.org/10.1016/j.jcou.2017.01.006.

[54] N.A. Zubbri, A.R. Mohamed, P. Lahijani, M. Mohammadi, Low temperature CO2 capture on biomass-derived KOH-activated hydrochar established through hydrothermal carbonization with water-soaking pre-treatment, J. Environ. Chem. Eng. 9 (2021) 105074, https://doi.org/10.1016/j.jece.2021.105074 –.

[55] Y. Guo, Q. Wang, Fabrication and characterization of activated carbon from phyllostachys edulis using single-step KOH activation with different temperatures, Processes 10 (2022) 1712, https://doi.org/10.3390/pr10091712.

[56] M.G. Plaza, A.S. González, C. Pevida, J.J. Pis, F. Rubiera, Valorisation of spent coffee grounds as CO2 adsorbents for postcombustion capture applications, Appl. Energy 99 (2012) 272–1229, https://doi.org/10.1016/j.apenergy.2012.05.028.
[57] G.K. Parshetti, S. Chowdhury, R. Balasubramanian, Biomass derived low-cost microporous adsorbents for efficient CO_2 capture, Fuel 148 (2015) 246–254, https://doi.org/10.1016/j.fuel.2015.01.032.
[58] H.M. Coromina, D.A. Walsh, R. Mokaya, Biomass-derived activated carbon with simultaneously enhanced CO_2 uptake for both pre and post combustion capture applications, J. Mater. Chem. A 4 (2016) 280–1229, https://doi.org/10.1039/C5TA09202G.
[59] Y. Sha, J. Lou, S. Bai, Wu. Da, B. Liu, Y. Ling, Facile preparation of nitrogen-doped porous carbon from waste tobacco by a simple pre-treatment process and their application in electrochemical capacitor and CO_2 capture, Mater. Res. Bull. 64 (2015) 327–332, https://doi.org/10.1016/j.materresbull.2015.01.015.
[60] Z. Zhang, K. Wang, J.D. Atkinson, X. Yan, X. Li, M.J. Rood, et al., Sustainable and hierarchical porous Enteromorpha prolifera based carbon for CO_2 capture, J. Hazard. Mater. 229–230 (2012) 183–191, https://doi.org/10.1016/j.jhazmat.2012.05.094.
[61] J. Song, W. Shen, J. Wang, W. Fan, Superior carbon-based CO_2 adsorbents prepared from poplar anthers, Carbon 69 (2014) 255–263, https://doi.org/10.1016/j.carbon.2013.12.024.
[62] L.K.G. Bhatta, S. Subramanyam, M.D. Chengala, U.M. Bhatta, N. Pandit, K. Venkatesh, Investigation of CO_2 adsorption on carbon material derived from *Mesua ferrea* L. seed cake, J. Environ. Chem. Eng. 3 (2015) 2957–2965, https://doi.org/10.1016/j.jece.2015.10.006.
[63] L. Domínguez-Ramos, A. Prieto-Estalrich, G. Malucelli, D. Gómez-Díaz, M.S. Freire, M. Lazzari, et al., N- and S-Doped carbons derived from polyacrylonitrile for gases separation, Sustainability 14 (2022) 3760, https://doi.org/10.3390/su14073760.
[64] D. Li, T. Ma, R. Zhang, Y. Tian, Y. Qiao, Preparation of porous carbons with high low-pressure CO_2 uptake by KOH activation of rice husk char, Fuel 139 (2015) 68–70, https://doi.org/10.1016/j.fuel.2014.08.027.
[65] M.M. Almoneef, H. Jedli, M. Mbarek, Experimental study of CO_2 adsorption using activated carbon, Mater. Res. Express 8 (2021) 065602, https://doi.org/10.1088/2053-1591/ac05fe.
[66] M. Mabuza, K. Premlall, M.O. Daramola, Modelling and thermodynamic properties of pure CO_2 and flue gas sorption data on South African coals using Langmuir, Freundlich, Temkin, and extended Langmuir isotherm models, Int. J. Coal Sci. Technol. 9 (2022) 1–15, https://doi.org/10.1007/s40789-022-00515-y.
[67] S. Chowdhury, R. Balasubramanian, Three-dimensional graphene-based porous adsorbents for postcombustion CO_2 capture, Ind. Eng. Chem. Res. Technol. 55 (2016) 7906–7916, https://doi.org/10.1021/acs.iecr.5b04052.
[68] J. Singh, S. Basu, H. Bhunia, CO_2 capture by modified porous carbon adsorbents: effect of various activating agents, J. Taiwan Inst. Chem. Eng. 102 (2019) 438–447, https://doi.org/10.1016/j.jtice.2019.06.011.
[69] J. Abdulsalam, J. Mulopo, S.O. Bada, B. Oboirien, Equilibria and isosteric heat of adsorption of methane on activated carbons derived from south African coal discards, ACS Omega 5 (2020) 32530–33259, https://doi.org/10.1021/acsomega.0c04744.
[70] K. Li, X. Niu, D. Zhang, H. Guo, X. Zhu, H. Yin, et al., Renewable biochar derived from mixed sewage sludge and pine sawdust for carbon dioxide capture, Environ. Pollut. 306 (2022) 119399, https://doi.org/10.1016/j.envpol.2022.119399.
[71] V. Selmert, A. Kretzschmar, H. Weinrich, H. Tempel, H. Kungl, R.-A. Eichel, CO_2/N_2 separation on highly selective carbon nanofibers investigated by dynamic gas adsorption, ChemSusChem 15 (2022), https://doi.org/10.1002/cssc.202200761.
[72] P. Billemont, N. Heymans, P. Normand, G. De Weireld, IAST predictions vs co-adsorption measurements for CO2 capture and separation on MIL-100 (Fe), Adsorption 23 (2017) 225–237, https://doi.org/10.1007/s10450-016-9825-6.
[73] N.F. Cessford, N.A. Seaton, T. Düren, Evaluation of ideal adsorbed solution theory as a tool for the design of metal−organic framework materials, Ind. Eng. Chem. Res. 51 (2012) 4911–4921, https://doi.org/10.1021/ie202219w.
[74] A.L. Myers, J.M. Prausnitz, Thermodynamics of mixed-gas adsorption, AIChE J. 11 (1965) 121–127, https://doi.org/10.1002/aic.690110125.
[75] E. Dautzenberg, S. van Hurne, M.M.J. Smulders, L.C.P.M. de Smet, GraphIAST: a graphical user interface software for Ideal Adsorption Solution Theory (IAST) calculations, Comput. Phys. Commun. 280 (2022) 108494, https://doi.org/10.1016/j.cpc.2022.108494.
[76] B. Liu, H. Li, X. Ma, R. Chen, S. Wang, L. Li, The synergistic effect of oxygen-containing functional groups on CO_2 adsorption by the glucose–potassium citrate-derived activated carbon, RSC Adv. 8 (2018) 38965–38973, https://doi.org/10.1039/C8RA05523H.
[77] M. Alhassan, M. Auta, J.K. Sabo, M. Umaru, A.S. Kovo, CO_2 capture using amine-impregnated activated carbon from Jatropha curcas shell, Br. J. Appl. Sci. Technol. 14 (2016) 1–11, https://doi.org/10.1039/C8RA05523H.
[78] S. Chowdhury, R. Balasubramanian, Three-dimensional graphene-based porous adsorbents for post-combustion CO_2 capture, Ind. Eng. Chem. Res. 55 (2016) 7906–7916, https://doi.org/10.1021/acs.iecr.5b04052.
[79] Y.-C. Chiang, C.-Y. Yeh, C.-H. Weng, Carbon dioxide adsorption on porous and functionalized activated carbon fibers, Appl. Sci. 9 (2019) 1977, https://doi.org/10.3390/app9101977.
[80] H. Li, J. Kang, F. Zhou, Z. Qiang, G. Li, Adsorption heat features of coalbed methane based on microcalorimeter, J. Loss Prev. Process Ind. 55 (2018) 437–449, https://doi.org/10.1016/j.jlp.2018.05.006.
[81] S. Jribi, T. Miyazaki, B.B. Saha, A. Pal, M.M. Younes, S. Koyama, A. Maalej, Equilibrium and kinetics of CO_2 adsorption onto activated carbon, Int. J. Heat Mass Transf. 108 (2017) 1941–11196, https://doi.org/10.1016/j.ijheattransfer.2016.12.114.
[82] S. Sircar, J.R. Hufton, Why does the linear driving force model for adsorption kinetics work, Adsorption 6 (2000) 137–147, https://doi.org/10.1023/A:1008965317983.
[83] Y.I. Aristov, Dynamics of adsorptive heat conversion systems: Review of basics and recent advances, Energy 205 (2020) 117998, https://doi.org/10.1016/j.energy.2020.117998.